Communications Biology

https://doi.org/10.1038/s42003-025-09363-3

Article in Press

Mitochondrial proteostasis regulated by CRL5^{Ozz} and Alix modulates skeletal muscle metabolism and fiber type

Received: 1 March 2025

Accepted: 27 November 2025

Cite this article as: Campos, Y., Palacios, G., Gomero, E. *et al.* Mitochondrial proteostasis regulated by CRL5^{Ozz} and Alix modulates skeletal muscle metabolism and fiber type. *Commun Biol* (2025). https://doi.org/10.1038/s42003-025-09363-3

Yvan Campos, Gustavo Palacios, Elida Gomero, Diantha van de Vlekkert, Krishnan Venkataraman, Jaison John, Jason Andrew Weesner, Randall Wakefield, Xiaohui Qiu, Ricardo Rodriguez-Enriquez, Stephanie Rockfield, Jeroen Demmers, Joseph T. Opferman, Cam Robinson, Khaled Khairy, Tulio Bertorini, Gerard C. Grosveld & Alessandra d'Azzo

Mitochondrial proteostasis regulated by CRL5^{Ozz} and Alix modulates skeletal muscle metabolism and fiber type

Yvan Campos[1,*,§,¶], Gustavo Palacios[2], Elida Gomero[1], Diantha Van de Vlekkert[1,#], Krishnan Venkataraman[3], Jaison John[3], Jason Andrew Weesner[1,5], Randall Wakefield[4], Xiaohui Qiu[1,#], Ricardo Rodriguez-Enriquez[5,‡], Stephanie Rockfield[5], Jeroen Demmers[6], Joseph T. Opferman[5], Cam Robinson[4], Khaled Khairy[3], Tulio Bertorini[7], Gerard C. Grosveld[1] and Alessandra d'Azzo[1,*,§]

[1]Department of Genetics, St. Jude Children's Research Hospital, 262 Danny Thomas Place, Memphis, Tennessee 38105, USA. [2]Department of Immunology, St. Jude Children's Research Hospital, 262 Danny Thomas Place, Memphis, Tennessee 38105, USA. [3]Center for Bioimage Informatics, St. Jude Children's Research Hospital, 262 Danny Thomas Place, Memphis, Tennessee 38105, USA. [4]Cell and Tissue Imaging Center, St. Jude Children's Research Hospital, 262 Danny Thomas Place, Memphis, Tennessee 38105, USA. [5]Department of Cell & Molecular Biology, St. Jude Children's Research Hospital, 262 Danny Thomas Place, Memphis, Tennessee 38105, USA. [6]Proteomics Center, Erasmus Medical Center, Wytemaweg 80, 3015 CN, Rotterdam, The Netherlands. [7]Department of Neurology, University of Tennessee Heath Science Center, Memphis, TN 38163, USA

[§]Lead contacts

*Correspondence: yvan.campos@stjude.org and sandra.dazzo@stjude.org

Abstract

High-energy-demanding tissues, such as skeletal muscle, rely on mitochondrial proteostasis for proper function. Two key quality-control mechanisms -the ubiquitin proteasome system (UPS) and the release of mitochondria-derived vesicles- help maintain mitochondrial proteostasis, but whether these processes interact remains unclear. Here, we show that $CRL5^{Ozz}$ and its substrate, Alix, localize to mitochondria and together regulate the levels and distribution of the mitochondrial solute carrier Slc25A4, which is essential for ATP production. In *Ozz*$^{-/-}$ or *Alix*$^{-/-}$ mice, skeletal muscle mitochondria exhibit similar morphological abnormalities, including swelling and dysmorphism, along with partially overlapping metabolomic alterations. We demonstrate that $CRL5^{Ozz}$ ubiquitinates Slc25A4, targeting it for proteasomal degradation, while Alix facilitates Slc25A4 loading into exosomes for lysosomal degradation. Loss of Ozz or Alix *in vivo* disrupts the steady-state levels of Slc25A4, impairing mitochondrial metabolism and triggering a switch in muscle fiber composition from oxidative, mitochondria-rich slow to glycolytic fast fibers.

Keywords: Mitochondria, Skeletal muscle, UPS, $CRL5^{Ozz}$, exosomes, Alix, Slc25A4, Mitochondria proteostasis, Mitochondria metabolism, muscle fiber types.

Main

The structure and function of skeletal muscle fibers are governed by their myosin composition and metabolic activity[1, 2]. Slow-twitch fibers (Type I) specialize in sustained, low-intensity contractions, and primarily rely on oxidative metabolism, while fast-twitch fibers (Type II) are optimized for rapid, powerful contractions, primarily fueled by glycolysis. These metabolic profiles are characterized by distinct ATP hydrolysis rates. A muscle fiber's metabolic capacity is influenced by factors such as capillarization, substrate availability, and mitochondrial density, all of which affect its energy production and efficiency[3]. During contraction, energy demands are met by the mitochondria, which generate ATP through oxidative phosphorylation (OXPHOS). In skeletal muscle, mitochondria form an interconnected reticular membrane network, often likened to a power grid[4, 5]. Based on their location within the muscle fiber, mitochondria are categorized as either subsarcolemmal or intermyofibrillar. Subsarcolemmal mitochondria exhibit notable plasticity, adjusting their volume through fusion and fission processes as needed, whereas intermyofibrillar mitochondria—though less morphologically adaptable—display higher rates of protein synthesis, enzyme activity, and respiratory efficiency[4, 5]. Furthermore, mitochondrial morphology—particularly elongated versus fragmented mitochondria—is closely linked to muscle fiber type and metabolic state[6]. Elongated and interconnected mitochondrial networks are typically enriched in oxidative fibers (type I and IIa), where they support sustained ATP production via OXPHOS. In contrast, fragmented or punctate mitochondria are more commonly associated with glycolytic fibers, which rely more heavily on anaerobic metabolism[6].

For optimal muscle fibers performance, mitochondria must maintain a balanced and functional proteome, a process regulated by the coordinated activity of several quality control (QC) mechanisms. These mechanisms include mitochondrial proteases found in both cytosolic and mitochondrial compartments, the ubiquitin proteasome system (UPS), and the release of cargo-loaded vesicles -such as mitochondrial-derived vesicles (MDVs)[7] and exosomes[8]- targeted for endolysosomal degradation[9]. Disruptions in any of these systems can lead to the accumulation

of misfolded, damaged, or aggregated mitochondrial proteins, ultimately causing cellular dysfunction and contributing to diseases such as mitochondrial myopathies and cardiomyopathies[10-12]. The UPS regulates the turnover of approximately 62% of the total mitochondrial proteome[13,14]**.** Key mitochondrial proteins targeted for UPS-mediated degradation include mitochondrial precursors essential for OXPHOS[15, 16], and those involved in maintaining organelle morphology[15, 16]. Several ubiquitinated mitochondrial proteins with identified ubiquitin ligases reside in the outer mitochondrial membrane (OMM), making them readily accessible to the proteasome[13, 17]. Still, for numerous proteins residing in the inner mitochondrial membrane (IMM)[18] or matrix, the identity of the responsible ubiquitin ligases and the mechanisms by which these proteins are extracted and targeted for proteasomal degradation are largely unclear[16]. The UPS operates with selectivity, targeting one ubiquitinated protein at a time. In contrast, MDVs and exosomes are enriched in mitochondrial proteins of diverse origins, most of which are destined for endolysosomal degradation, although the mechanisms that govern their selective sorting into these nanovesicles remain elusive. MDV cargo includes components of the translocase of the outer membrane (TOM) complex and subunits of the mitochondrial electron transport chain[19]. Similarly, exosomes have been found to contain TOM complex proteins, mitochondrial solute carriers (Slc), and other mitochondrial-derived proteins[20-23]. However, it is still debatable the extent to which MDVs resemble exosomes in their origin, characteristics, and function**.**

In addition to these QC systems, cells employ mitophagy as an independent surveillance mechanism to eliminate irreversibly damaged or dysfunctional mitochondria through lysosomal degradation[24-27]. This regulated process, essential for cell survival, involves multiple interrelated pathways activated in response to various physiological and pathological stimuli. A well-characterized form of mitophagy involves the de novo formation of autophagosomes at or near the surface of stressed mitochondria and the activation of the ubiquitin pathway via PINK1 and Parkin[24-27]. Notably, PINK1 and Parkin have also been implicated in the biogenesis of MDVs suggesting an interplay between MDV formation, endolysosomal degradation, and mitophagy[22,

[28, 29]. A key question that remains is whether these distinct mitochondrial QC mechanisms operate independently or function cooperatively, particularly in maintaining skeletal muscle homeostasis.

Ozz, also known as Neuralized-like protein 2 (Neurl2), is highly expressed in skeletal and cardiac muscle, where it functions as the substrate-recognition component of $CRL5^{Ozz}$ — a muscle-specific Cullin RING-type ubiquitin ligase complex composed of Elongin B/C, Rbx1, and Cul5[30, 31]. The primary structure of Ozz consists of two NHR (Neuralized Homology Repeat) domains, which are responsible for substrate recognition, and a C-terminal SOCS box that mediates interaction with the Elongin B/C complex[30, 31]. The NHR domains are defining features of the Neuralized protein family, which comprises mammalian orthologs and paralogs of *Drosophila* Neuralized (*D*Neur)[32, 33]. In mammals, this family comprises Neur1 (also known as Neurl1a) and Neur2 (or Neurl1b), which, like *D*Neur, are expressed in the brain. Additional members include, Ozz (Neurl2), LINCR (or Neurl3) and KIAA1787 (or Neurl4)[32, 33]. Except for Ozz, which functions as part of a CRL complex, the other four members act as monomeric RING-type E3 ubiquitin ligases. These proteins differ in their tissue distribution and substrate specificity[32, 33]. $Ozz^{-/-}$ mice exhibit pronounced sarcomeric defects, such as misaligned, split, or branched myofibrils and disorganized Z-discs. These findings suggest a critical role for $CRL5^{Ozz}$ and its substrates in the formation and/or maintenance of the sarcomeric apparatus during embryogenesis, as well as in muscle differentiation/regeneration[31, 34]. During early embryogenesis, Ozz is detected in the somites, at the tips of myotomal cells, near the intermyotomal septum, and within myotendinous junctions[31]. As myofiber differentiation progresses, Ozz expression gradually increases, initially localizing to the tips of the differentiating myocytes before becoming distributed throughout the mature fiber[31]. Consistently, $CRL5^{Ozz}$ substrates are present in various subcellular compartments of the myofibers and include sarcomeric proteins, membrane proteins, and the multidomain, scaffold protein, Alix.

Alix, also referred to as programmed cell death 6-interacting protein (PDCD6IP), is a key component of two large multiprotein complexes: the ESCRT (endosomal sorting complexes

required for transport) and the F-actin cytoskeleton[35-45]. Through these associations, Alix takes part in various cellular processes, including multivesicular body sorting, and exosome biogenesis[35, 36, 38-41, 43, 45, 46]. Previously, we reported that silencing *Alix* expression in C2C12 myoblasts alters F-actin levels and distribution, reduces membrane protrusion formation, and impairs extracellular vesicle release[35, 47]. In *Alix*$^{-/-}$ mice, the most prominent phenotype resulting from Alix deficiency is severe and progressive hydrocephalus caused by defective assembly and positioning of the actomyosin-tight junction complex in the choroid plexus epithelium. This Alix-dependent process is essential for maintaining epithelial cell polarity and the integrity of the epithelial barrier[37]. However, it remains to be determined whether Alix, as a substrate of CRL5^{Ozz}, plays a specific role in skeletal muscle and, if so, whether its deficiency *in vivo* affects myofibers in a manner similar to Ozz deficiency.

In this study, we explore these questions by examining how Ozz, as substrate recognition component of CRL5^{Ozz}, and Alix, as mediator of cargo-loading into exosomes, function together in specific skeletal muscle types. Through genetic, proteomic, and 3D imaging approaches, we demonstrate that Ozz and Alix localize to the mitochondria, where they regulate the degradation of a common substrate, the solute carrier, Slc25A4 (also known as ANT1). Loss of Ozz or Alix in mouse skeletal muscle reciprocally influences each other's roles as mitochondrial QC systems: Ozz deficiency increases the pool of exosome-loaded Slc25A4, while Alix deficiency redirects Slc25A4 to proteasomal degradation. Despite these compensatory mechanisms to regulate Slc25A4 abundance in mitochondria, the loss of either protein fails to mitigate mitochondrial stress, resulting in impaired mitochondrial metabolism and a metabolic switch in myofibers from OXPHOS to glycolysis.

RESULTS

Ozz and Alix localize to mitochondria, and their individual loss disrupts mitochondrial morphology

Given that Alix is a substrate of $CRL5^{Ozz}$ we aimed to determine whether the loss of Alix in skeletal muscle would lead to myofiber defects similar to those observed in the skeletal muscle of the original *Ozz*$^{-/-}$ mouse line[31]. To investigate this, we first analyzed the expression levels and spatial distribution of Alix relative to Ozz in lysates from various wild-type (WT) skeletal muscle types (Supplementary Fig. 1a). While no significant differences in the expression levels of either protein were detected on immunoblots (Supplementary Fig. 1a), immunofluorescent staining of muscle sections revealed prominent Alix localization in the soleus, which is rich in slow-twitch (Type I) fibers, as well as in the adjacent gastrocnemius region that also contains Type I fibers (Supplementary Fig. 1b). The Ozz protein was distributed throughout the myofibers, while Alix was predominantly localized beneath the sarcolemma, with faint presence inside the myofibers (Supplementary Fig. 1c). Hematoxylin and eosin (H&E)-stained cross sections of the *Alix*$^{-/-}$ soleus muscle revealed gross abnormalities closely resembling those observed in the *Ozz*$^{-/-}$ muscle, including numerous small-caliber fibers and fibers with central nuclei (Supplementary Fig. 1d). At the ultrastructural level, *Alix*$^{-/-}$ myofibers also displayed misaligned sarcomeric units and altered Z-band streaming, both characteristic features of *Ozz*$^{-/-}$ myofibers (Fig. 1a).

Surprisingly, both models exhibited similar mitochondrial dysmorphisms, characterized by mitochondria of irregular shape, size, and number (Fig. 1b and Supplementary Fig. 2a). However, we did not observe a clear bias toward either overtly elongated or fragmented mitochondria in the mutant muscles. Instead, mitochondrial morphologies appeared heterogeneous and disorganized, consistent with a dysregulated mitochondrial network. These observations prompted us to investigate whether Ozz and Alix localize to mitochondria. Indeed, both proteins were detected in purified mitochondrial preparations from WT skeletal muscle. However, in mitochondria isolated from *Alix*$^{-/-}$ and *Ozz*$^{-/-}$ muscles, the levels of each protein increased in the

absence of the other (Fig. 1c), suggesting a reciprocal regulatory relationship between these proteins within mitochondria. To further explore their submitochondrial distribution, purified mitochondria from WT, *Alix*$^{-/-}$, and *Ozz*$^{-/-}$ skeletal muscles were subjected to protease treatment and alkaline extraction, followed by immunoblotting with specific antibodies. Proteinase K treatment, degraded Ozz and Alix (Fig. 1d), along with Tom20, a known OMM protein, while Slc25A4, an IMM resident protein, was unaffected (Fig. 1d). All proteins, including Slc25A4, remained intact when mitochondria were subjected to osmotic shock with potassium chloride (KCl). However, when KCl and proteinase K were combined, Ozz, Alix, and Tom20 were degraded, whereas Slc25A4 remained intact. Treatment with SDS (sodium dodecyl sulfate) and proteinase K led to the degradation of all proteins, regardless of their localization (Fig. 1d). These findings confirm that Ozz and Alix localize to the OMM. To determine whether these proteins associate with the luminal or cytosolic side of the OMM or are embedded within the OMM, we incubated purified mitochondria with trypsin. This treatment completely digested Ozz, Alix, and Tom 20 (Fig. 1d). Additionally, alkaline treatment removed Ozz and Alix from the OMM but did not affect Tom20 (Fig. 1d). These results suggest that Ozz and Alix associate with the OMM, topologically facing the cytosolic side, without being embedded in the membrane. Consequently, our findings indicate that, like Ozz, Alix plays a role in maintaining sarcomeric integrity and preserving mitochondrial homeostasis.

Ozz contains a mitochondrial targeting sequence

Using the Mitoprot software (https://ihg.gsf.de/ihg/mitoprot.html), we identified a putative mitochondrial-targeting sequence (MTS) within the primary sequence of Ozz, but not Alix. This MTS consists of 36 amino acids located within the first NHR domain (Fig. 1e). To validate this finding, we generated *Ozz* mutant mice using CRISPR/Cas9, introducing deletions of two, five, or nine amino acids (Δ2aa, Δ5aa, and Δ9aa) at the N terminus of the MTS (Fig. 1e). Deletion of five or nine amino acids abolished Ozz localization to muscle mitochondria, whereas trace amounts

of the Δ2aa protein were still detected (Fig. 1f). These results confirm that the MTS motif in Ozz is essential for its mitochondrial localization. Additionally, we generated a CRISPR/Cas9 mutant mouse, *ccOzz*$^{-/-}$, carrying a single base pair deletion that introduced a stop codon eight amino acids downstream of the start site (Fig. 1e). This mouse served as a control for all CRISPR/Cas9-derived mutants and was used in all subsequent experiments.

Histopathologic examination of the soleus muscles from all deletion mutants revealed gross morphologic defects, consistent with those observed in the original Ozz$^{-/-}$ mice[31] (Fig. 1a, b). H&E staining (Supplementary Fig. 2b) and toluidine blue-stained muscle sections (Supplementary Fig. 2c) from the Δ5aa, Δ9aa, and *ccOzz*$^{-/-}$ mice showed numerous small-caliber fibers, disrupted striation patterns, and increased presence of immature fibers with central nuclei. The Δ2aa mice appeared to be the least affected (Supplementary Fig. 2c). However, ultrastructural analysis revealed that all mutant mice, including the Δ2aa, exhibited the same myofiber abnormalities as seen in the *Alix*$^{-/-}$ and *Ozz*$^{-/-}$ models (Fig. 2d), including sarcomere misalignment, abnormal Z-band streaming, and defective mitochondria (Supplementary Fig. 2d, e).

3D Segmentation of Mitochondria in *Alix*$^{-/-}$ and *ccOzz*$^{-/-}$ soleus muscles

To further evaluate the altered mitochondrial morphology observed in *Alix*$^{-/-}$ and *ccOzz*$^{-/-}$, we analyzed the mitochondrial network structure in skeletal muscle (Fig. 2a). Using machine learning-based image analysis software, we delineated the mitochondrial outer membrane, enabling 3D segmentation and rendering of individual mitochondria. This allowed us to quantify key structural parameters, including volume, surface area, and sphericity (Fig. 2). In WT soleus muscle, intermyofibrillar mitochondria (n≅2000) were densely packed, predominantly exhibiting an elongated, ellipsoid-like shape with their long axis aligned along the myofibrils (Fig. 2a, b and Supplementary movie 1). The average mitochondrial volume was ~3x10^6 nm^3 (Fig. 2c), with an

average surface area of ~1.8x10^5 nm^2 (Fig. 2d) and an average sphericity of 0.5 (Fig. 2e). In contrast, mitochondria in *Alix*$^{-/-}$ (n≅1200) (Fig. 2a, b and Supplementary movie 2) and *ccOzz*$^{-/-}$ (n≅1400) (Fig. 2 a, b and Supplementary movie 3) muscles displayed striking morphological alterations, appearing swollen and dysmorphic. Additionally, their average volume (Fig. 2C), surface areas (Fig. 2d) and sphericity (Fig. 2e) were notably different from those in WT muscle. To further investigate mitochondrial differences, we performed quantitative PCR on total DNA isolated from the soleus muscles of three males and two females WT, *Alix*$^{-/-}$ and *ccOzz*$^{-/-}$ mice, comparing the relative mitochondrial DNA (mtDNA) copy number to nuclear DNA across these samples. Despite variability among samples from different mice within each group (Supplementary Fig. 3a and Supplementary table 1), the analysis revealed that the mtDNA copy number relative to nuclear DNA was higher in WT muscle (~939) compared to *Alix*$^{-/-}$ (~860) and *ccOzz*$^{-/-}$ muscle (~849). However, these differences did not reach statistical significance, likely due to sample heterogeneity. Overall, these findings align with the mitochondrial counts obtained from the 3D segmentation analysis.

Mitochondrial respiration is reduced in *Alix*$^{-/-}$and *Ozz*$^{-/-}$ skeletal muscles

The deficiency of Ozz or Alix appeared to similarly affect mitochondrial morphology. To further characterize this phenotype in both models, we investigated whether these structural changes were associated with impaired mitochondrial function. We first assessed the oxygen consumption rate (OCR), a key indicator of mitochondrial bioenergetic capacity, in primary myoblast cultures (Day 0) and differentiated myocytes/myotubes (Day 3) derived from WT, *Alix*$^{-/-}$, and *ccOzz*$^{-/-}$ limb muscles (Fig. 3a, b). While all three OCR profiles were similar in shape, the amplitudes for *Alix*$^{-/-}$ and *ccOzz*$^{-/-}$ samples at Day 3 were significantly lower than those of WT controls. Basal mitochondrial respiration, normalized by subtracting non-mitochondrial OCR, was reduced 2-fold in *Alix*$^{-/-}$ myotubes and 3-fold in *ccOzz*$^{-/-}$ myotubes compared to WT (p = 0.0001). (Fig. 3b).

Oligomycin A inhibition revealed that proton leak was similar across all cells, indicating that most basal mitochondrial respiration in both WT and mutant cells was dedicated to ATP production (Fig. 3b). Treatment with the mitochondrial-uncoupler FCCP, which transports protons across the IMM, independent of ATP synthase, allowed measurements of maximum oxygen consumption (Fig. 3b). This analysis showed an even greater reduction in OCR in *Alix*$^{-/-}$, *ccOzz*$^{-/-}$ myotubes compared to WT (p <0.0001) (Fig. 3b). Among the mutants, *ccOzz*$^{-/-}$ myotubes exhibited the lowest respiratory reserve capacity (p =0.0001), while *Alix*$^{-/-}$ myotubes had intermediate values (p <0.0006), suggesting that Ozz plays a greater role than Alix in maintaining mitochondrial respiratory capacity. Similar OCR profiles were observed in proliferating *Alix*$^{-/-}$ and *ccOzz*$^{-/-}$ myoblasts at Day 0 (Supplementary Fig. 4a, b).

To assess mitochondrial membrane potential (ΔΨm), we used the TMRE probe in proliferating and differentiating *Alix*$^{-/-}$ and *ccOzz*$^{-/-}$ myoblasts and myotubes. TMRE is a cell-permeant fluorescent dye that accumulates in mitochondria with an intact ΔΨm; its fluorescence decreases when ΔΨm dissipates, indicating a loss of mitochondrial membrane integrity. Our analysis revealed that mean TMRE fluorescence intensity in *ccOzz*$^{-/-}$ myotubes was reduced by ~20% compared to WT (p=0.0092) (Fig. 3c). However, no significant difference in ΔΨm was observed between the *Alix*$^{-/-}$ and WT myotubes (Fig. 3c).

To determine whether proteasomal inhibition mimics the ΔΨm defect observed in the absence of Ozz, we treated WT, *Alix*$^{-/-}$ and *ccOzz*$^{-/-}$ Day 3 myotubes with MG132 and measured mitochondrial ΔΨm (Fig. 3c). MG132 treatment reduced ΔΨm by ~50% in WT and *Alix*$^{-/-}$ myotubes (p <0.0001), and by ~60% in cc*Ozz*$^{-/-}$ myotubes (p <0.0001) compared to untreated controls (Fig. 3c). These findings suggest that general inhibition of proteasomal degradation leads to ΔΨm dissipation, similar to the effect observed in *ccOzz*$^{-/-}$ myotubes. However, the same analysis in proliferating myoblasts showed no significant differences among WT, *ccOzz*$^{-/-}$, and *Alix*$^{-/-}$ cells (Supplementary Fig. 4c).

Given the decreased ΔΨm, particularly in *ccOzz*$^{-/-}$ Day 3 myotubes, we sought to determine whether the OXPHOS pathway was affected. To investigate this, we analyzed the steady-state levels of OXPHOS proteins in mitochondrial preparations from WT, *Alix*$^{-/-}$ and *ccOzz*$^{-/-}$ limb muscles (Fig. 3d). Immunoblot analyses with antibodies against subunits of complexes I-V showed no significant differences in protein composition between *Alix*$^{-/-}$ and *ccOzz*$^{-/-}$ mitochondria compared to the WT controls (Fig. 3d).

Finally, we investigated whether the functional mitochondrial defects in *ccOzz*$^{-/-}$ and, to a lesser extent, *Alix*$^{-/-}$ myotubes were associated with histochemical changes in the muscle tissue, as typically observed in human mitochondrial myopathies[10, 12]. For this purpose, we applied three standard mitochondrial staining methods (modified Gomori trichrome, succinate dehydrogenase [SDH] and cytochrome C [Cyt C]) to cross-sections of soleus muscle from adult WT, *Alix*$^{-/-}$and *ccOzz*$^{-/-}$ mice. Gomori trichrome staining in *Alix*$^{-/-}$and *ccOzz*$^{-/-}$ muscles revealed an increased number myofibers with deep red-color, ragged contours and a subsarcolemmal dye accumulation, indicative of mitochondrial myopathy (Supplementary Fig. 4d). Additionally, a higher number of fibers in these muscles exhibited intense staining with SDH and cyt C, suggesting increased mitochondrial enzymatic activity in the *ccOzz*$^{-/-}$and *Alix*$^{-/-}$ soleus muscles (Supplementary Fig. 4d).

Mitochondrial dysfunction in *Alix*$^{-/-}$ and *ccOzz*$^{-/-}$ skeletal muscle induces mitophagy

The mitochondrial defects observed in *Alix*$^{-/-}$ and *ccOzz*$^{-/-}$ soleus muscles suggest overall mitochondrial dysfunction, which may trigger selective mitophagy under physiological conditions[48-50]. To test this possibility, we crossed *Alix*$^{-/-}$ and *ccOzz*$^{-/-}$ mice with the *mito*-QC reporter mouse model, which expresses a GFP-mCherry construct targeted to mitochondria[51]. In this model, mitophagy activation is assessed by counting the number of red-only puncta, which represent autophagosomes containing engulfed mitochondria that have fused with acidic lysosomes, thereby quenching the GFP fluorescence signal[51]. Confocal microscopy of soleus

muscle cross-sections from these crosses revealed a significant increase in red-only puncta in *mito*-QC/*Alix*$^{-/-}$ and *mito*-QC/*ccOzz*$^{-/-}$ mice compared to WT controls (Figs. 4a, b and Supplementary Fig. 5). These findings suggest that the loss of Ozz or Alix in skeletal muscle induces mitophagy as a consequence of mitochondrial dysfunction.

Metabolomics of *Alix*$^{-/-}$ and *ccOzz*$^{-/-}$ soleus muscles reveal mitochondrial insufficiencies

The functional and biochemical mitochondrial defects observed in *Alix*$^{-/-}$ and *ccOzz*$^{-/-}$ myofibers may indicate an overall impaired mitochondrial metabolism. To investigate this further, we conducted high-throughput metabolomic analyses on soleus muscles from 8-week-old male and female *Alix*$^{-/-}$, *cc*Ozz$^{-/-}$, and WT mice (Supplementary table 2). Our analysis identified 87 metabolites with significantly altered levels in the *Alix*$^{-/-}$ and *ccOzz*$^{-/-}$ soleus muscles (Supplementary data 1, 2) compared to WT muscle. Using MetaboAnalyst software, we generated heat maps illustrating the differential metabolite levels in each mutant muscle relative to the WT control (Fig. 5a, b). Combining the heat map values for each metabolite revealed distinct metabolic profiles for *Alix*$^{-/-}$, *ccOzz*$^{-/-}$, and WT soleus muscles (Fig. 5b). Remarkably, several of the identified metabolites – such as ADP, citrate, Citrulline, CoA, FAD, L-Acetylcarnitine, carnitine, oxoglutarate, and PEP (Supplementary data 2) were found to be regulated by the mitochondrial SLC25 solute carrier family of proteins[52-55]. Pathway analysis of metabolites altered in *Alix*$^{-/-}$ and *ccOzz*$^{-/-}$ soleus muscles revealed changes in mitochondrial- and muscle-related pathways, including glycolysis, the TCA cycle, pyrimidine metabolism, the pentose phosphate pathway, and acetyl group transfer (Fig. 5c, d; Supplementary table 3, 4, Supplementary data 3, **ST004190**). Notably, both overlapping and distinct pathways were identified in the two knockout models, underscoring a combination of shared and unique metabolic disruptions (Fig. 5c, d, pathways marked in bold). Upregulation of the pyrimidine pathway suggests increased nucleotide availability, which may support the enhanced rate of mitochondrial replication and repair. This is further evidenced by the altered mitochondrial DNA copy number in *Alix*$^{-/-}$, *ccOzz*$^{-/-}$ muscles

compared to WT muscle, as well as the increased number of mitochondria observed at the ultrastructural level (Supplementary table 1 and Supplementary Fig. 2a). Conversely, the altered metabolites associated with glycolysis, TCA, the pentose phosphate pathway[56], and the transfer of acetyl groups to mitochondria in the *Alix*$^{-/-}$ and *ccOzz*$^{-/-}$ muscles suggest metabolic adaptation in the skeletal muscle of both mutant mice (Fig. 5c,d, Supplementary table 3 and 4).

To confirm the increase in glycolysis in the *Alix*$^{-/-}$ and *ccOzz*$^{-/-}$ muscles, we measured their glycolytic rate using the Seahorse XF assay in Day 3 myotubes, comparing it to WT muscle. This method provides a more precise assessment than measuring glycolytic acidification alone. Pyruvate, a product of glucose catabolism, can either be converted to lactate in the cytoplasm or enter the TCA cycle in the mitochondria, where it is oxidized to CO_2 and water. Glycolytic lactate and mitochondria-derived CO_2 are the primary contributors to the proton efflux rate (PER), leading to extracellular acidification. The proportion of PER attributed to glycolysis (% PER from glycolysis) varies across different cell types. In highly oxidative cells, such as slow-twitch myofibers, it is crucial to account for mitochondria-derived CO_2 acidification when measuring extracellular acidification by lactate to accurately assess glycolysis. The Seahorse XF assay enable this by simultaneously measuring the extracellular acidification rate (ECAR) from both mitochondrial and glycolytic sources. This allows for the calculation of GlycoPER by subtracting the mitochondrial CO_2-derived PER from the total PER (Fig. 5e). Our analysis revealed that basal glycolysis, measured as GlycoPER, was elevated in *Alix*$^{-/-}$ and *ccOzz*$^{-/-}$ myotubes compared to WT myotubes (Fig. 5f). Following the addition of the mitochondrial electron transport chain inhibitor rotenone/antimycin A, compensatory glycolysis increased similarly in WT, *Alix*$^{-/-}$, or *ccOzz*$^{-/-}$ myotubes, with not significantly differences in all samples (Fig. 5e, g). However, the % PER from glycolysis was significantly higher in *Alix*$^{-/-}$($p=0.0006$) and *ccOzz*$^{-/-}$ myotubes ($p<0.0001$) (Fig. 5h). These findings indicate that glycolysis is upregulated in *Alix*$^{-/-}$ and *ccOzz*$^{-/-}$ myotubes, coinciding with a significant impairment in mitochondrial basal respiration (Supplementary Fig. 6a).

To better quantify changes in individual metabolites associated with glycolysis and the TCA cycle, we conducted gas chromatography-mass spectrometry (GC-MS) on soleus muscles and D3 myotubes from WT, *Alix*$^{-/-}$ and *ccOzz*$^{-/-}$ mice. This analysis revealed elevated levels of TCA cycle metabolites - including citrate, α-ketoglutarate, succinate, fumarate, and malate - in *Alix*$^{-/-}$ and *ccOzz*$^{-/-}$ samples compared to WT controls (Supplementary Fig. 6b, c). The accumulation of these metabolites in mutant muscles further supports the notion of altered OXPHOS, which is compensated by increased glycolysis.

Deficiency of Ozz or Alix *in vivo* induces a switch in muscle fiber type

To further explore the altered mitochondrial metabolism in the skeletal muscles of *Alix*$^{-/-}$ and *ccOzz*$^{-/-}$ mice, we investigated the relationship between fiber-type composition and fiber-energy metabolism in the soleus muscle. This muscle is predominantly composed of slow oxidative Type I fibers, characterized by high levels of slow myosin heavy chain (slow MyHC), and fast oxidative/glycolytic Type IIA fibers, characterized by MyHC-IIA expression. We used MyHC expression as a standard parameter to assess myofiber heterogeneity, although recent transcriptomic data indicate that myofiber heterogeneity arises from multidimensional variations involving proteins beyond MyHC isoforms[57]. MyHC expression levels were analyzed in serial cross-sections of soleus muscles from *Alix*$^{-/-}$, *ccOzz*$^{-/-}$, and WT mice by immunofluorescent staining for MyHC isoforms Type I and Type IIA. Using an ImageJ macro program, we were able to distinguish fiber types based on their fluorescent staining patterns and quantify each fiber type. In the WT soleus muscle, the expected distribution was observed, with 46% slow Type I fibers and 54% fast Type IIA fibers (Fig. 6a, b). The *Alix*$^{-/-}$ soleus muscle contained 42% slow Type I fibers and 58% fast Type IIA fibers, while the Ozz$^{-/-}$ soleus muscle contained only 32% slow Type I fibers and 68% fast Type IIA fibers (Fig. 6a, b). Both mutant muscles showed an increased percentage of glycolytic/oxidative Type IIA fibers at the expense of oxidative Type I fibers.

However, the Ozz deficiency was more pronounced, resulting in a 30% reduction in Type I fibers compared to a ~9% reduction in the *Alix*$^{-/-}$ muscle.

We then examined whether the myosin expression pattern correlated with the functional ATPase activity of individual myofibers. For this, we applied a metachromatic myofibrillar ATPase staining method to frozen serial sections of soleus muscles from *Alix*$^{-/-}$, *ccOzz*$^{-/-}$, and WT mice. This method distinguished three fiber types based on color intensity: Type I oxidative fibers (light blue), Type IIA glycolytic/oxidative fibers (intermediate blue), and Type IIX glycolytic fibers (dark blue) (Fig. 6c, d). Using a similar ImageJ macro program, we quantified the fiber types. The WT soleus muscle consisted of approximately 31% oxidative Type I fibers, 33% glycolytic/oxidative Type IIA fibers, and 36% glycolytic Type IIX fibers (Fig. 6c, d). In contrast, the *Alix*$^{-/-}$ soleus muscle contained about 28% oxidative Type I fibers, 31% glycolytic/oxidative Type IIA fibers, and a comparable 36% glycolytic Type IIX fibers. The *ccOzz*$^{-/-}$ soleus muscle was the most affected, containing only ~24% oxidative Type I fibers, with increased percentages of glycolytic/oxidative Type IIA (35%) and glycolytic Type IIX (41%) fibers.

These analyses further confirm that deficiency of Alix or Ozz induces a switch in myofiber composition in the soleus muscle towards the glycolytic type.

CRL5^{Ozz} in mitochondria targets the solute carrier Slc25A4 for proteasomal degradation

Having established the mitochondrial localization of Ozz, we next sought to determine whether the other components of CRL5^{Ozz} also co-localized in this organelle. We first tested whether endogenous EloC, EloB, Rbx1, and Cul5 could be detected through co-immunoprecipitation and/or immunoblotting of mitochondria isolated from WT, *Alix*$^{-/-}$, or *ccOzz*$^{-/-}$ skeletal muscle. These initial experiments were unsuccessful, likely due to the low expression levels of Ozz and Alix in steady-state mitochondria. To address this, we overexpressed recombinant Ozz fused to a short peptide tag (Avi-tag), which was biotinylated by the co-expressed bacterial ligase BirA[58, 59]. Cells transduced with an empty vector were used as controls. Mock-transduced and Avi-Ozz–

overexpressing C2C12 myotubes (Day 3) were incubated with streptavidin beads to capture biotinylated Avi-Ozz and any interacting proteins. Immunoblot analysis of the pulled proteins showed that Avi-Ozz was associated with all other components of the $CRL5^{Ozz}$ ligase as well as Alix, indicating that biotinylated Avi-Ozz assembled into an active E3 ligase (Supplementary Fig. 7a). Aliquots of the streptavidin-captured proteins were also subjected to mass spectrometry, confirming the pull-down of Ozz's direct interactors, EloB and EloC. Interestingly, several members of the mitochondrial solute carrier family, including the muscle-specific Slc25A4, were also pulled down with Ozz, suggesting that these proteins could be potential substrates for $CRL5^{Ozz}$-mediated proteasomal degradation.

We then tested whether we could detect an assembled $CRL5^{Ozz}$ in crude mitochondrial preparations from differentiated C2C12 cells that were either mock-transduced or overexpressing biotinylated Avi-Ozz (Fig. 7A). Immunoblots of these mitochondrial extracts (input) showed the presence of Tom20 and Slc25A4 (Fig. 7a). Moreover, Ozz, Alix, and Rbx1 were detected in cells overexpressing Avi-Ozz, while EloB, EloC, and Cul5 were barely visible (Fig. 7a). However, after performing a streptavidin pull-down of biotinylated Avi-Ozz, we observed all components of $CRL5^{Ozz}$, as well as Alix and Slc25A4 (Fig. 7a), confirming the assembly of this ligase in mitochondria and its interaction with Slc25A4. The fact that Tom20 was also pulled down with Ozz (Fig. 7a) suggests that Ozz's localization to the mitochondria may be regulated by direct or indirect interaction with the TOM complex. To further validate that Slc25A4 interacts with Ozz *in vivo*, we immunoprecipitated mitochondrial lysates from gastrocnemius and soleus muscles using anti-Slc25A4 antibodies and probed the blots with an anti-Ozz antibody (Fig. 7a). Ozz co-immunoprecipitated with Slc25A4 from both WT and $Alix^{-/-}$ mitochondrial lysates, demonstrating that these endogenous proteins physically associate with each other (Fig. 7a).

To confirm that Slc25A4 is a bona fide substrate of $CRL5^{Ozz}$, we performed in vitro ubiquitination assays using a purified, reconstituted $CRL5^{Ozz}$ complex and a GST-tagged full-length recombinant Slc25A4 (Fig. 7c). The ubiquitinated products were then probed on

immunoblots with anti-ubiquitin, anti-Slc25A4, and anti-GST antibodies (Fig. 7c). These in vitro reactions revealed the polyubiquitination of Slc25A4, confirming it as a substrate of $CRL5^{Ozz}$ (Fig. 7c). To further verify whether $CRL5^{Ozz}$ recognizes native or denatured Slc25A4, we performed a second in vitro ubiquitination assay using either native or heat-denatured substrate (Fig. 7d). This assay demonstrated that thermally denatured Slc25A4 was no longer ubiquitinated by $CRL5^{Ozz}$ (Fig. 7d), indicating that $CRL5^{Ozz}$ specifically recognizes the native form of Slc25A4.

Alix regulates the loading of mitochondrial Slc25A4 into exosomes

Since both Alix and Slc25A4 were identified in a pull-down experiment using biotinylated Avi-Ozz from differentiated myotubes, we aimed to investigate whether Alix directly interacts with Slc25A4. To test this, we used mitochondrial fractions isolated from C2C12 cells overexpressing FLAG-tagged full-length Alix. Our results showed that FLAG-tagged Alix co-immunoprecipitated with Slc25A4, suggesting that these two proteins interact within mitochondria (Fig. 7f). Additionally, Alix co-immunoprecipitated with Tom20, indicating a potential physical interaction between these proteins, possibly mediated by three Tom20-recognition motifs located within Alix's Bro1 domain (Fig. 7e, f). However, further investigation is needed to confirm this hypothesis.

Considering Alix's role in cargo sorting and the biogenesis of multivesicular body/exosomes, we next examined the contents of extracellular vesicles/exosomes isolated from *Alix*$^{-/-}$, *ccOzz*$^{-/-}$, and WT gastrocnemius/soleus muscles. Purified vesicles were fractionated on sucrose density gradients, and the resulting fractions were analyzed by immunoblotting with antibodies against exosomal markers CD9 and CD81, as well as mitochondrial markers Tom20 and Tom70 (Supplementary Fig. 7g and 7b). The fractionation pattern of CD81 indicated that exosomes from all experimental groups sedimented in gradients at fractions 3-7, with densities ranging from 1.10 to 1.14 g/mL[60] (Supplementary Fig. 7b). Notably, Ozz, Alix, and Slc25A4 were detected in WT exosomes, though at relatively low levels (Supplementary Fig. 7b). Due to the variability observed in protein levels across individual fractions, which stemmed from

inconsistencies in trichloroacetic acid precipitation, we pooled fractions 1-2 (F1), corresponding to heavy vesicles enriched in endolysosomal markers, and fractions 3-7 (F2), which represented the exosomal fractions (Fig. 7g).

However, immunoblot analysis of the pooled fractions F1 and F2 revealed that not only Ozz and Alix, but also Slc25A4, were present in exosomes from WT muscles (Fig. 7g). Interestingly, the absence of either Ozz or Alix led to the accumulation of the remaining protein in both exosomal pools (Fig. 7g). Additionally, Slc25A4 levels were reduced in exosomes from *Alix*$^{-/-}$ muscles but increased in exosomes from *ccOzz*$^{-/-}$ muscles (Fig. 7g and Supplementary Fig. 7c). Based on these results, we infer that impaired CRL5^{Ozz}-mediated degradation of Slc25A4 in *ccOzz*$^{-/-}$ muscle redirects the protein to exosomes, while the absence of Alix leads to inefficient loading of Slc25A4 into exosomes (Fig. 7g and Supplementary Fig. 7c). We also assessed the levels and distribution of Slc25A4 in the mitochondrial and cytosolic fractions isolated after exosome extraction from WT, *Alix*$^{-/-}$, and *ccOzz*$^{-/-}$ muscles (Fig. 7h). As expected, most of the Slc25A4 was found in the mitochondrial fractions rather than the cytosolic fractions, consistent with its function as a solute carrier in mitochondria (Fig. 7h). However, when comparing the levels of Slc25A4 in the mitochondrial fractions from *Alix*$^{-/-}$ and *ccOzz*$^{-/-}$ muscles with those from WT muscle, we observed that Slc25A4 levels were reduced in the mitochondria of the mutants but increased in their corresponding cytosolic fractions. This suggests a shift in the overall distribution of Slc25A4 in mutant skeletal muscle (Fig. 7h and Supplementary Fig. 7d). Lastly, since CRL5^{Ozz} is associated with the OMM (Fig. 1d), it is likely that CRL5^{Ozz} targets the cytosolic pool of Slc25A4 for proteasomal degradation at this site, thereby regulating the amount of Slc25A4 that is imported into the mitochondria.

DISCUSSION

Mitochondria utilize diverse QC systems to maintain proteostasis, a tightly regulated process activated in response to various stimuli to preserve overall cellular and organ function. In this

study, we identify a crucial role for the multimeric E3 ligase, CRL5^{Ozz}, and its substrate, Alix, in skeletal muscle mitochondria. We show that CRL5^{Ozz}, a member of the UPS, and Alix, which mediates cargo-loading into exosomes, collaboratively regulate the mitochondrial levels of the solute carrier, Slc25A4. Specifically, CRL5^{Ozz} promotes Slc25A4 proteasomal degradation, while Alix facilitates its loading into exosomes, highlighting a coordinated mechanism for mitochondrial proteostasis. Deficiency of Ozz or Alix in skeletal muscle disrupts the mitochondrial balance of this solute carrier, which is preferentially directed to the proteasome in absence of Alix, or to exosomes in absence of Ozz, though the molecular mechanisms governing this switch remain unknown. We speculate that this disturbed Slc25A4 proteostasis contributes to the numerous mitochondrial dysmorphisms observed in both deficient mouse models, suggesting a functional interplay between these QC systems. Mitochondrial dysmorphisms, including irregular mitochondrial shape, size and number, likely reflect a metabolic adaptation of the muscle fibers. These mitochondrial defects disrupt the efficiency of the electron transport chain and consequently impair mitochondrial ATP production via the TCA cycle[61-63]. As a compensatory response, glycolysis is upregulated to meet the energy demands of slow-twitch muscle fibers, whose ATP requirements are normally met predominantly through aerobic mitochondrial respiration under wild-type conditions. Biochemically, we found that *ccOzz*$^{-/-}$ mitochondria exhibit reduced OCR and dissipation of the ΔΨm. While these defects are also observed in *Alix*$^{-/-}$ mitochondria, they are comparatively less severe. These histopathological and biochemical abnormalities in the skeletal muscle of both mouse models indicate significant mitochondrial stress, which consequently triggers increased mitophagy. However, it is important to keep in mind that the MitoQC approach we have used to monitor mytophagy is only one readout of this process; additional mitophagy detection methods, such as measuring mitophagic flux, should be considered in the future for better interpreting this phenotype in both mouse models.

We demonstrate that deficiency of Ozz or Alix impacts skeletal muscle metabolism and fiber composition, specifically in slow-twitch muscle. In humans, skeletal muscle fibers are highly

plastic; their composition can vary significantly depending on the muscle group and physiological context[64, 65]. Typically, human skeletal muscle comprises a heterogeneous mix of fiber types, with an approximate balance of 50% Type I (oxidative) and 50% Type II (glycolytic), the latter of which includes subtypes IIa, IIb, and IIx[1, 2]. Type I fibers are specialized for sustained aerobic activity, characterized by a high mitochondrial content and a predominant reliance on OXPHOS for energy production. Instead, Type II (IIx and IIb) fibers contain fewer mitochondria and depend more on anaerobic ATP production through glycolysis[2, 66]. Type IIa fibers exhibit hybrid characteristics between Type I and Type IIb fibers, possessing an intermediate number of mitochondria and oxidative capacity[2, 66]. In contrast, mouse skeletal muscle is more homogeneous, with a predominance of Type IIb and IIx fibers; Type IIa fibers are less common, and Type I fibers are primarily restricted to specific muscles, such as the soleus. Given that both Ozz and Alix are highly expressed in Type I fibers (Supplementary Fig. 1), we focused our fiber-type analyses on the soleus muscle. Our findings reveal that the loss of Alix or Ozz in this muscle induces changes in MyHC isoform composition, leading to a metabolic switch from OXPHOS toward glycolysis. This metabolic switch is further supported by the increased levels of metabolites associated with glycolytic myofibers in both mutant soleus muscles, accompanied by a reduction in those linked to oxidative myofibers. Notably, several of these metabolites (e.g., ADP, citrate, Citrulline, CoA, FAD, L-Acetylcarnitine, carnitine, oxoglutarate, and PEP) are regulated by members of the SLC25 family of mitochondrial solute carriers. These transporters, including SLC25A4, facilitate the exchange of amino acids, carboxylic acids, fatty acids, cofactors, inorganic ions, and nucleotides across the IMM and are essential for numerous cellular functions[52-55], particularly those governing mitochondrial oxidative balance. Among them, SLC25A4 is one of the most abundant isoforms and is highly expressed in cardiac and skeletal muscles[67].

Approximately 62% of the mitochondrial proteome is regulated and turned over by the UPS, and 49% of all ubiquitinated proteins are localized exclusively to the mitochondria[14]. Multiple components of the UPS are localized to the OMM, where they ubiquitinate mitochondrial proteins

that need to be extracted from the mitochondrial membrane and positioned to face the cytosol to be translocated and degraded by the proteasome[13, 17]. This process is proposed to be mediated by mitochondrial-associated degradation (MAD), which is analogous to the endoplasmic-reticulum-associated degradation (ERAD) pathway[68, 69]. During MAD, the Cdc48/VCP/p97 ATPase, together with various cofactors, recognizes and dislodges ubiquitinated proteins from the OMM, directing them toward proteasomal degradation[17]. In addition to OMM substrates, several inner mitochondrial membrane (IMM) proteins, such as uncoupling proteins UCP2 and UCP3[70-72], as well as SLC25A4 (identified in this study), are also polyubiquitinated and degraded via the proteasome. However, it remains unclear whether this degradation occurs within the mitochondria or whether these IMM substrates undergo retro-translocation into the cytosol via the MAD pathway prior to proteasomal degradation[13, 70]. The targeting of IMM proteins, including SLC25A4, by the UPS represents an intriguing and underexplored aspect of mitochondrial proteostasis that warrants further investigation.

As an antiporter, SLC25A4 facilitates the exchange of ADP and ATP across the IMM, a process driven by the ΔΨm that regulates the cytosolic ATP/ADP ratio. Cells with high aerobic metabolic demands, such as neurons, cardiomyocytes, and hepatocytes, maintain a higher ATP/ADP ratio in the cytosol than in the mitochondrial matrix[73], which suppresses glycolysis[74-76]. However, when mitochondrial function is impaired, ATP production declines, leading to a dramatic drop in the cytosolic ATP/ADP ratio and a compensatory metabolic shift towards glycolysis for ATP generation. Our findings demonstrate that in skeletal muscle, the loss of Alix or Ozz disrupts the steady-state levels of Slc25A4, impairing mitochondrial ΔΨm and driving an increased reliance on glycolysis.

In humans, SLC25A4 expression increases during myoblast differentiation[77], a pattern of expression shared by Ozz. Notably, the *Slc25A4*$^{-/-}$ mouse model[78] develops mitochondrial defects in skeletal muscle that resemble those seen in *Alix*$^{-/-}$ and *ccOzz*$^{-/-}$ skeletal muscles, including enlarged and dysmorphic mitochondria - features characteristic of ragged-red fibers

commonly found in human mitochondrial myopathies. Biochemically, mitochondria of *Slc25A4*$^{-/-}$ skeletal muscle exhibit defects in ADP-stimulated respiration, which align with impaired ATP/ADP transport across the IMM[78]. In contrast to Slc25A4 deficiency in mice, *in vitro* overexpression of this carrier leads to saturation of the mitochondrial import machinery in the cytosol, causing protein accumulation and aggregation. These results in mitochondrial precursor overaccumulation stress, or mPOS, which is characterized by the toxic buildup of unimported mitochondrial proteins in the cytosol, increased protein ubiquitination, and apoptotic cell death[79, 80]. In humans, mutations in the *SLC25A4* gene are linked to mitochondrial diseases[81]. Dominant heterozygous mutations in *SLC25A4* are associated with adult-onset autosomal-dominant external ophthalmoplegia, a multisystemic disorder characterized by skeletal muscle weakness[67, 82] and mitochondrial DNA deletions that reduce the mtDNA copy number to ~5-34%[81]. This feature is also observed in *Alix*$^{-/-}$ and *ccOzz*$^{-/-}$ skeletal muscle. Conversely, recessive *SLC25A4* mutations lead to childhood-onset mitochondrial myopathy and cardiomyopathy[81].

Despite significant progress in understanding the molecular foundations of mitochondrial myopathies, the etiology of many such conditions remains unclear. Our findings position Ozz and Alix as potential predisposing factors for idiopathic myopathies in humans. However, due to the species-specific differences in muscle fiber composition and plasticity, caution should be exercised when extrapolating these results to human physiology.

ACKNOWLEDGMENTS

We would like to thank Dr. George Campbell of the St. Jude Cell and Tissue Imaging Center for help with image acquisitions. We gratefully acknowledge Dr. Tommaso Nastasi for his valuable contributions during the initial phase of this project and Dr. Angela McArthur (St. Jude Department of Scientific Editing) for editing the manuscript. The C57BL/6-Gt(ROSA)26Sor$^{tm1(CAG-mCherry/GFP)Ganl}$/GanlH mice were obtained from the MRC Harwell Institute which distributes this strain on behalf of the European Mouse Mutant Archive (EMMA: www.infrafrontier.eu). The repository number is EM:11343. The C57BL/6-Gt(ROSA)26Sor$^{tm1(CAG-mCherry/GFP)Ganl}$/GanlH mice were originally produced at The University of Dundee. A. d'Azzo holds an endowed chair in Genetics and Gene Therapy from the Jewelry Charity Fund. This study was funded in part by the National Institutes of Health grants AR049867, GM104981 and CA021764, the Assisi Foundation of Memphis, and the American Lebanese Syrian Associated Charities (ALSAC). The content is solely the responsibility of the authors and does not necessarily represent the official views of the National Institutes of Health.

AUTHOR CONTRIBUTION

Y.C. conceived the study, designed the experiments, analyzed the data, generated the mouse models, coordinated the efforts of all authors, and drafted the manuscript. G.P. designed, performed and analyzed the soleus metabolomics and TCA data, and helped with the interpretation of the data and explanation of the methodology. E.G. maintained the animal colonies and performed surgeries. D.v.d.V. performed the isolation, purification and analyses of exosomes from WT and mutant muscles, and helped with statistical analyses, and the editing of the manuscript and figures. K.V, J. J., and K. K. performed the 3D segmentation, rendering and statistical analyses of muscle mitochondria from WT and mutant mice. J.W. wrote the macros for ImageJ/Fiji software used to analyze and quantify mitophagy, to determine the MyHC content in

myofibers from WT and mutant muscles and to quantify ATPase activity in different fiber types. R. W. and C. R. obtained and processed TEM and SEM images. R.R. and S.R. helped with the mitochondrial OCR assays and the analyses of ΔΨm. X.Q. purified anti-Ozz and anti-Alix antibodies, prepared and maintained primary myoblast cultures and performed Alix overexpression studies in C2C12 cells. J.D. performed proteomic analyses of C2C12 overexpressing tagged Ozz. J.T.O. and T.B. provided intellectual insights. G.C.G. provided intellectual insights, advised on the CRISPR/CAS9 mutagenesis and edited the manuscript. A. d'A. conceived the study, designed the experiments, analyzed the data, oversaw all experiments, coordinated the efforts of all authors, secured the funding for this project and wrote and edited the manuscript.

DECLARATION OF INTERESTS

The authors declare no competing interests.

FIGURE LEGENDS

Fig. 1. Abnormal myofibril organization and mitochondria in *Alix*$^{-/-}$ and *Ozz*$^{-/-}$ mice

(a) Transmission electron microscopy (TEM) of soleus muscle dissected from *Alix*$^{-/-}$ and *Ozz*$^{-/-}$ mice revealed a misalignment of sarcomeres with dysmorphic mitochondria compared to WT. Scale bar: 1 μm.

(b) TEM of soleus muscle dissected from *Alix*$^{-/-}$, *Ozz*$^{-/-}$, and WT mice revealed defective mitochondrial morphology and size. Scale bar: 200 nm.

(c) Immunoblot analyses of the mitochondrial (2 μg) and cytosolic (6 μg) fractions of *Alix*$^{-/-}$, *Ozz*$^{-/-}$, and WT soleus muscles revealed endogenous Ozz and Alix. The purity of the subcellular fractionation of membranes & organelles was verified by immunoblotting using antibodies against a mitochondrial fraction marker (anti-ATPB) and an endoplasmic reticulum marker (anti-calreticulin).

(d) Purified mitochondria were subjected to protease digestion before or after high-salt treatment, followed by immunoblot analyzes with anti-Ozz, anti-Alix, anti-Tom20 (OMM), and anti-Slc25A4[18] antibodies.

(e) Identification of a mitochondrial-targeting sequence in the Ozz protein's primary structure. The numbers refer to amino acid (aa) positions, starting from the N-terminal end. Alignment of the Ozz aa sequence of mutant mice with that of WT mice confirmed the deletion of 2, 5, and 9 aa in exon 1 of the Ozz protein generated by the CRISPR/Cas9 system.

(f) Immunoblot analyses of purified mitochondria probed with anti-Ozz antibody showed the absence of Ozz in ∆5aa, ∆9aa, and *ccOzz*$^{-/-}$ muscle, whereas the ∆2aa muscle showed trace amounts of Ozz.

Fig. 2, Imaging and Quantitative Analysis of Mitochondrial Morphology in WT, *Alix*$^{-/-}$ and *ccOzz*$^{-/-}$ soleus skeletal muscle

(a) 3D reconstructed images of intermyofibrillar mitochondria in soleus skeletal muscle from WT, *Alix*$^{-/-}$, and *ccOzz*$^{-/-}$ emphasizing distinct mitochondrial shapes, volumes. and distributions.

(b) 3D rendering and segmentation of intermyofibrillar mitochondria display the diverse appearance of mitochondrial in WT, *Alix*$^{-/-}$, and *ccOzz*$^{-/-}$ soleus skeletal muscles. The different colors depict the individual mitochondria.

(c) Comparison of volume average (nm^3) of mitochondria quantifications.

(d) Comparison of the surface of mitochondria (nm^2) in WT, *Alix*$^{-/-}$, and *ccOzz*$^{-/-}$ muscle.

(e) Comparison of the sphericity of mitochondria in WT, *Alix*$^{-/-}$, and *ccOzz*$^{-/-}$ muscle.

Data are presented as median ± quartiles, One-Way ANOVA; WT: n≅2000, *Alix*$^{-/-}$: n≅1200, and ccOzz$^{-/-}$: n≅1200.

Fig. 3. Analysis of mitochondrial phenotype in *Alix*$^{-/-}$ and *ccOzz*$^{-/-}$ skeletal muscle

(a) Oxygen consumption rate (OCR) profile of primary myotubes of WT, *Alix*$^{-/-}$, and *ccOzz*$^{-/-}$ mice (Day 3) in response to treatment with oligomycin (ATP-linked respiration and proton leak), FCCP (mitochondrial reserve capacity), and rotenone/antimycin A (nonmitochondrial respiration). Hoechst 33342 staining was used to count the number of cells.

(b) Analysis of the different stages of myoblast respiration determined from the OCR analysis in A of WT, *Alix*$^{-/-}$, and *ccOzz*$^{-/-}$ primary myotubes (Day 3). Data are presented as mean ± SD, Student's (unpaired) *t*-test; n = 3 independent samples.

(c) Quantitative analysis of $\Delta\Psi M$ by using the mean fluorescence intensity (MFI) of TMRE in the primary myotubes of WT, *Alix*$^{-/-}$, and *ccOzz*$^{-/-}$ muscle in non-treated and treated with 50 µM of MG132 for 3h. Data are presented as mean ± SD, Student's (unpaired) *t*-test; n = ~8000 cells per n = 3 independent samples.

(d) Representative Western blot of mitochondrial OXPHOS complexes (CI: NDUFB8, CII: SDHB, CIII: UQCRC2, CIV: MTCO1, CV: ATP5A) in mitochondria preparation from WT, *Alix*$^{-/-}$, and *ccOzz*$^{-/-}$ limb muscle.

Fig. 4. Mitophagy analysis using MitoQC reporter mice

(a) Representative confocal images of the soleus muscle isolated from MitoQC/WT, MitoQC/*Alix*$^{-/-}$ and MitoQC/*ccOzz*$^{-/-}$ mice show increased mitophagy (red) in both MitoQC/*Alix*$^{-/-}$ and MitoQC/*ccOzz*$^{-/-}$ mice. Scale bars: 5 µm.

(b) Quantification of mitochondria engulfed by the lysosome (red-only puncta). Total number of red-only puncta per area of muscle fiber. Data are presented as median ± quartiles, One-Way ANOVA; puncta per average number of fibers or average area, WT: n=3, Alix: n=3, Ozz: n=3 mice.

Fig. 5. Enrichment of metabolic pathways in *Alix*$^{-/-}$ and *ccOzz*$^{-/-}$ soleus skeletal muscle

(a) Clustered heat map of metabolites detected at significantly different ($p < 0.05$) levels between *Alix*$^{-/-}$ (n = 4) or *ccOzz*$^{-/-}$ (n = 6) and WT control (n = 4) soleus muscle samples.

(b) Clustered heat map (grouped) of the top 41 metabolites detected at significantly different ($p < 0.05$) levels between *Alix*$^{-/-}$ (n = 4) or *Ozz*$^{-/-}$ (n = 6) and WT control (n = 4) soleus muscle samples.

(c) Functional enrichment and pathway topology analysis of metabolites affected in *Alix*$^{-/-}$ soleus muscle compared to WT control by using the MetaboAnalyst 6.0-Join Pathway Analysis tool (The color and size of each circle correspond to its P-value and enrichment factor, respectively. Darker red tones indicate greater statistical significance of the metabolites associated with the corresponding metabolic pathway (i.e. lower P-values). In contrast, the size of each dot (node) reflects the pathway impact factor, which is calculated based on the number of metabolites hits relative to the total number of compounds in each metabolic pathway node).

(d) Functional enrichment and pathway topology analysis of metabolites affected in *ccOzz*$^{-/-}$ soleus muscle compared to WT control by using the MetaboAnalyst 6.0-Joint Pathway Analysis tool (The color and size of each circle correspond to its P-value and enrichment factor, respectively. Darker red tones indicate greater statistical significance of the metabolites associated with the corresponding metabolic pathway (i.e. lower P-values). In contrast, the size of each dot (node) reflects the pathway impact factor, which is calculated based on the number of metabolites hits relative to the total number of compounds in each metabolic pathway node).

(e) Analysis of the glycolytic rate assay in. WT, *Alix*$^{-/-}$ and *ccOzz*$^{-/-}$ D3 myotubes. ECARs, OCRs at basal level and after the addition of ROT/AA and 2-deoxy-D-glucose (2-DG) were monitored in real time by using the Seahorse XF Glycolytic Rate Assay and converted to the PERs.

(f) Increased Basal Glycolytic capacity in *ccOzz*$^{-/-}$ D3 myotubes. Data represented as mean ± SEM of n = 3 individual samples.

(g) The compensatory glycolytic capacity in both *Alix*$^{-/-}$ and *ccOzz*$^{-/-}$ D3 myotubes were not statistically significant compared to that of the WT.

(h) Increased Glycolysis (%PER) capacity in *Alix*$^{-/-}$ and *ccOzz*$^{-/-}$ D3 myotubes.

Fig. 6. Fiber-type switching in muscles of *Alix*$^{-/-}$ and *ccOzz*$^{-/-}$ mice

(a) Immunofluorescence staining of soleus muscle sections from WT, *Alix*$^{-/-}$, and *ccOzz*$^{-/-}$ mice with antibodies specific for MyHC Type I (red) or MyHC Type IIA (green) fibers. Scale bar: 100 μm.

(b) Quantification of the average percentage of Type I and Type IIA fibers from panel A. Data are presented as mean ± SD, Student's (unpaired) *t*-test; n = 4 independent samples.

(c) Representative images of metachromatic ATPase staining on cross sections of soleus muscle from WT, *Alix*$^{-/-}$, and *ccOzz*$^{-/-}$ mice. ATPase activity stains Type I fibers (dark blue), Type IIA fibers (light blue), and Type IIB fibers (very light blue). Scale bar: 200 μm

(d) Quantification of the average percentage of Type I (oxidative), Type IIA (glycolytic/oxidative) and Type IIX (glycolytic) fibers from panel C. Data presented are the mean ± SD, Student's (unpaired) *t*-test; n = 4 independent samples.

Fig. 7. Alix and Ozz cooperatively regulate Slc25A4

(a) Biotinylated mitochondrial Avi-Ozz from preparations of C2C12 myotubes (Day 3) were analyzed by Western blot using antibodies to detect CRL5^{Ozz} ligase components (EloB, EloC, Cul5, Rbx1), Alix substrates/interactors, Slc25A4, Tom20, and Avi-Ozz protein.

(b) Immunoprecipitation (IP) of mitochondrial lysates isolated from WT, *Alix*$^{-/-}$, and *ccOzz*$^{-/-}$ muscles showed co-precipitation of Slc25A4 and Ozz. Immunoblots were probed with anti-Ozz and anti-Slc25A4 antibodies.

(c) In vitro ubiquitination of GST-Slc25A4, followed by Western blot analysis with anti-ubiquitin (UBQ), anti-Slc25A4 and anti-GST antibodies.

(d) In vitro ubiquitination of denatured, denature insoluble and non-denatured GST-Slc25A4, followed by Western blot analysis with anti-ubiquitin (UBQ), anti-Slc25A4 and anti-GST antibodies.

(e) Protein domain mapping of Tom20-recognition motifs (orange boxes) identified in the Alix primary protein structure. The numbers refer to the amino acid positions starting from the N-terminal sequence of Alix protein.

(f) IP of purified FLAG-tagged Alix from C2C12 myotubes (Day 3) probed with anti-Alix, anti-Ozz, anti-Slc25A4, and anti-Tom20 antibodies showed the interaction of Slc25A4 with Alix.

(g) Immunoblot analyses of pooled sucrose-gradient fractions of exosomes (F1: fractions 1-2 and F2: fractions 3-6) isolated from WT, *Alix*$^{-/-}$, and *ccOzz*$^{-/-}$ muscles probed with antibodies against Alix, Ozz, Slc25A4, CD9, Tom20, and Tom70.

(h) Immunoblot analyses of mitochondrial and cytosolic fractions after exosomes preparation of *Alix*$^{-/-}$, *ccOzz*$^{-/-}$, and WT muscles probed with antibodies against Alix, Ozz, and Slc25A4 revealed differences in the localization of endogenous Ozz, Alix and Slc25A4.

METHODS

Mice

Mice of all genotypes were housed in the Animal Resource Center at St. Jude Children's Research Hospital. WT mice were C57Bl/6xDBA2 (B6D2F1; Jackson Labs); *Alix*$^{-/-}$[37] and *Ozz*$^{-/-}$[31] mice carried homozygous deletions of Alix or Ozz, respectively, on the same B6D2F1 background. Animals were maintained in a fully AAALAC-accredited (Association for Assessment and Accreditation of Laboratory Animal Care) facility, with food and water provided *ad libitum*. All experimental procedures were conducted in accordance with protocols approved by the St. Jude Institutional Animal Care and Use Committee and followed NIH guidelines and we have complied with all relevant ethical regulations for animal use.

Generation of Ozz$^{-/-}$ mice via CRISPR/Cas9

To engineer *ccOzz*$^{-/-}$ mice via CRISPR/Cas9, we synthesized a single-guide RNA (sgRNA, 5′-GCTGCTCCCTCCGAACACGT-3′) from linear DNA templates (IDT DNA) using the TranscriptAid T7 High Yield Transcription Kit (Thermo Fisher Scientific). The sgRNA was purified according to the manufacturer's instructions. Purified sgRNA (50 ng/μL) was microinjected into the pronucleus of fertilized embryos derived from Rosa26-Cas9 knock-in female mice (The Jackson Laboratory). Viable embryos were transferred into the oviducts of pseudopregnant B6D2F1 females (C57BL/6 × DBA2; The Jackson Laboratory). Homozygous *ccOzz*$^{-/-}$ mice were obtained from heterozygous intercrosses and used for phenotypic analyses, alongside age- and sex-matched wild-type (WT) littermates as controls.

Detection of genetic modification by PCR

To assess the genomic modification of *Ozz*-CRISPR/Cas9, we isolated genomic DNA from tail biopsies and used it as a template for PCR. The samples were digested in 200 μL of 50 mM NaOH and incubated at 98 °C for 1 hour. Samples were neutralized with 20 μL of 1M Tris-HCl

(pH 8.0), and PCR analysis was performed with 1 µL genomic DNA in a 50-µL mixture containing 1× Green GoTaq Reaction Buffer (PROMEGA), 10 mM dNTP mix (Thermo Fisher Scientific), 50 pMol of each primer Ozz-For 5'-GTGACAAGCGAGAAAGCGGCGC-3' and Ozz-Rev 5'-CTGCCTCCGCTTCTGGTTGACC-3' and 1.25 U of recombinant Taq polymerase (Thermo Fisher Scientific). The PCR conditions were as follows: initial denaturation (94 °C for 3 min), 34 cycles of denaturation (94 °C for 30 s), annealing (61 °C for 30 s), extension (72 °C for 1 min), and a final extension at 72 °C for 10 min. The PCR products were run on agarose gels, purified using a gel extraction kit (QIAGEN), and sequenced to determine the location of the mutation. To discriminate between the different mutations, we subcloned the PCR products of selected sequences and amplified them in bacteria (WHS-one). DNA was extracted from single clones by using a MiniPrep Extraction Kit (QIAGEN) and Sanger-sequenced. CRISPR/Cas9 mutant mice were genotyped as follows: 8-µL PCR reactions were incubated for 2 h at 37 °C, in a mixture of 2 µL 10× Cutsmart buffer, 1 µL BsaAI enzyme (New England Biolabs), and 9 µL water. The digested products were visualized on 2% agarose gel stained with SYBR SAFE DNA gel stain (Thermo Fisher Scientific). Gels were imaged using a ChemiDoc MP Imaging System (Bio Rad).

Antibodies and reagents

Anti-Ozz (In house WB: 1/500, IF: 1/50)[31], Anti-Alix (In house WB: 1/500, IF: 1/50)[35], Anti-SLC25A4 1/1000 (SAB Signaling Antibody-32484), Anti-Elongin B (WB: 1/200, Santa Cruz sc-11447), Anti-Elongin C (WB: 1/300, Transduction Laboratories-610761), Anti-Cullin 5 (WB: 1/200, Santa Cruz sc-13014), Anti-Rbx1 (WB:1/500, NeoMarkers-069-P1ABX), Anti-Ubiquitin (WB: 1/500, Invitrogen-131600), Anti-Tom20 (WB: 1/500, Abcam-ab186735), Anti-Tom70 (WB: 1/500, Proteintech-14528-1-AP), Anti-CD81 (WB: 1/200, Santa Cruz-sc-166029), Anti-CD9 (WB: 1/500, BD Transduction Laboratories-553758), Anti-Flotillin (WB: 1/500, BD Transduction Laboratories-610820), Anti-LC3 (WB: 1/500 Sigma-Aldrich-L7543), Anti-β-catenin (WB 1/500, BD Transduction Laboratories-610154), Anti-MyHC IIA (IF: 1:50, DSHB-SC-71), Anti-MyHC IIB (IF: 1:50, DSHB-

BF-F3), Anti-MyHC slow (IF: 1:50, DSHB-BA-D5), Anti-Skeletal muscle actin (WB:1/1000, Abcam-52218), Anti-F-actin (WB: 1/500, Abcam-Ab205), Anti-Cdc42 (WB: 1/500, Novus-NBP1-45477), Anti-GST (WB: 1/500, Santa Cruz-Sc-138), Anti-Calreticulin (WB: 1/1000, Cell Signaling 12238), Anti-ATPB (WB: 1/1000, Abcam-ab14730), and OXPHOS (WB: 1/500, Abcam-ab110413). Other commercial antibodies included: Normal rabbit IgG (Cell Signaling-2729S), Normal mouse IgG (Cell Signaling-5415S), Goat anti-mouse IgG1, Alexa Fluor 488 (Invitrogen-A21121), Goat anti-mouse IgG2b, Alexa Fluor 555 (Invitrogen-A21147), Goat anti-mouse IgM, Alexa Fluor 647 (Invitrogen-A21238), Peroxidase AffiniPure Goat anti–mouse IgG (Jackson ImmunoResearch-115-035-146), Peroxidase AffiniPure Goat anti–rabbit IgG Jackson ImmunoResearch (111-035-144) and Alexa Fluor 488-conjugated anti-rabbit (Invitrogen-A21206). Reagents: Anti-FLAG M2 magnetic beads (Millipore-M8823), Biotin (Invitrogen-B20656), Collagen (Sigma-Aldrich-C9791), KCl (Fisher-P217-500), Proteinase K (Ambion-AM2546), Trypsin (Sigma-Aldrich-T6567), Dynabeads Streptavidin (Invitrogen-11205D), GammaBind Plus Sepharose (Cytiva-17088601), Calcium chloride dihydrate (Sigma-Aldrich-C3306), Toluidine blue O (Sigma-Aldrich-T3260), 2-amino-2-methyl-1-propanol (Sigma-Aldrich-08578), Potassium acetate (Fisher-BP364-500), Tris-base (Invitrogen-15504-020), Adenosine 5'-triphosphate disodium salt hydrate (Sigma-Aldrich-A7699), MG132 (Sigma-Aldrich-474790-1MG), E1 (Enzo-BML-UW941U-0050), E2 (Enzo-BML-UW9060-0100), 10X ATP (Enzo-12091903), 10X Ubiquitylation buffer (Enzo-BML-KW9885-001) and Ubiquitin (Bio-Techne-U-100H).

Tissue preparation for cryosectioning

Dissected soleus or gastrocnemius muscle was embedded in 2%Tragacanth/1× PBS and flash-frozen for 10 s in isopentane cooled in liquid nitrogen. Tissues were stored at −80 °C until sectioning. Coronal or longitudinal serial sections of frozen muscles were cut on a cryostat (Leica CM3050) and adhered to superfrost plus microscope slides for immunofluorescence (8 µm) or

SDH, Cyt C, and ATPase staining (12 µm). Slides were stored at –20 °C. The sections were also stained with H&E for overall morphologic assessment.

Toluidine blue staining

Soleus dissected muscles were postfixed in 1% OsO_4 and *en bloc* stained with 1% uranyl acetate. After standard dehydration, samples were infiltrated and embedded in Spurr low-viscosity resin (Electron Microscopy Sciences) and polymerized at 60 °C for 18 h. Semithin sections (1.5 µm) were cut and dried overnight at 45 °C. For toluidine blue staining, sections were placed on a heating tray at 95 °C, 0.1% toluidine blue was added, and the sections were incubated for 1 min. The slides were washed twice for 1 min in 95% ethanol and twice for 1 min in 100% ethanol. The sections were then cleared twice for 3 min in xylene before they were covered with paramount. Images were acquired on a Nikon C2 confocal microscope using NIS Elements software.

Electron microscopy

Mice (aged 1–2 months) were anesthetized using Avertin (0.5 mg/g body weight) and perfused with 4% paraformaldehyde. The soleus or gastrocnemius muscles were dissected and postfixed in 2.5% glutaraldehyde in 0.1 M sodium cacodylate buffer. Both muscles were cut into small pieces, postfixed in 2% osmium tetroxide, and dehydrated via a graded series of alcohol. They were then cleared in propylene oxide, embedded in epon araldite, and polymerized overnight at 70 °C. Sections (70-nm thick) were cut on a Leica Ultracut E. The unstained sections were imaged on a JEOL 1200 EX transmission electron microscope with an AMT 2K digital camera.

Serial Block Face Scanning Electron Microscopy

Two-month-old mice were anaesthetized using Avertin (0.5 mg g−1) and perfused with 4% paraformaldehyde. Following perfusion, soleus muscles were dissected and postfixed in 2.5% glutaraldehyde, 2% paraformaldehyde in 0.1M cacodylate buffer. Following fixation, samples

were prepared for volume imaging as in Hua et al[83], omitting the lead aspartate staining. Samples were post-fixed in 2% osmium tetroxide in cacodylate buffer for 90 minutes at room temperature and then transferred directly to 2.5% potassium ferrocyanide in cacodylate buffer. Samples were thoroughly rinsed with ddH2O and incubated at 40°C for 45 minutes in 1% thiocarbohydrazide and again thoroughly washed prior to being incubated in 2% aqueous osmium tetroxide at room temperature for 90 minutes. Samples were rinsed with ddH2O and incubated in 1% aqueous uranyl acetate overnight at 4°C then warmed to 50°C for 30 minutes, held at room temperature for 1 hour and returned to 50°C for 30 minutes. Following thorough rinsing with ddH2O, samples were dehydrated in an ascending series of ethanol, transitioned in propylene oxide and infiltrated with EMBed-812 epoxy resin. Samples in 100% EMBed-812 were polymerized at 60°C for 2 days. Selected samples were mounted, trimmed, and coated with iridium for imaging in a Thermo Fisher Scientific Helios FIBSEM. Imaging conditions were adjusted on a per sample basis to ensure consistent imaging and milling. Individual scan series consisted of roughly 500–1000 serial sections acquired at a nominal voxel resolution of 2.7 x 2.7 x 10 nm.

Mitochondria Segmentation:

Mitochondria from wild type and KO volumes were first segmented using a fine-tuned cell pose model[84, 85]. Model “cyto2” (fine-tuned using three hundred two-dimensional z-sections), was used to produce a rough initial segmentation for the two-dimensional slices of the volume. A six-directional connected component analysis was performed to combine these segmentations into a three-dimensional volume. Mitochondria were labeled using a majority vote. Finally, artifacts were removed by volume filtering (< 25000 cu. nm). The volume was then visualized in napari[86]

Mitochondria Metrics Extraction:

Volume, surface area and sphericity were calculated for each mitochondrion. For calculating the surface area, surface meshes were generated using the Marching cubes algorithm[87]. For calculating the sphericity metric, the formula devised by Wadell[88] was applied.

Preparation of crude or pure mitochondria from muscle tissue

Pure mitochondria were isolated using a modified version of the protocol described by Wieckowski et al.[89]. In brief, mice were euthanized by CO_2 inhalation, and the soleus and gastrocnemius muscles were dissected and immediately washed in 2 mL of ice-cold IB3 buffer (225 mM mannitol, 75 mM sucrose, 30 mM Tris-HCl, pH 7.4), then stored in fresh ice-cold IB3 buffer. The muscles were minced into very small pieces using scalpels and transferred to a 5-mL glass homogenizer. Samples were homogenized in 2 mL (1:5 ratio to tissue weight) of ice-cold IB1 buffer (225 mM mannitol, 75 mM sucrose, 30 mM Tris-HCl, pH 7.4, 0.5% BSA, 0.5 mM EGTA) using a Teflon pestle (8 strokes). Homogenates were transferred to 5-mL Eppendorf centrifuge tubes and centrifuged at 700 ×g for 5 min at 4 °C. The pellets were discarded, and the supernatants were centrifuged again at 700 ×g for 5 min at 4 °C. The resulting supernatants were transferred to new tubes and centrifuged at 9,000 ×g for 10 min at 4 °C. The resulting pellets, containing crude mitochondria, were gently resuspended in 2 mL of ice-cold IB2 buffer (225 mM mannitol, 75 mM sucrose, 30 mM Tris-HCl, pH 7.4, 0.5% BSA) using a Dounce homogenizer.

The crude mitochondrial suspensions were further centrifuged at 10,000 ×*g* for 10 min at 4 °C, and the resulting pellets were gently resuspended in 2 mL IB3 buffer. The suspensions were centrifuged again at 10,000 ×*g* for 10 min at 4 °C, and the crude mitochondrial pellets were resuspended in 2.5 mL ice-cold mitochondrial reaction buffer (MRB; 250 mM mannitol, 5 mM HEPES [pH 7.4], 0.5 mM EGTA) by using a Dounce homogenizer. The crude mitochondrial suspensions were layered over an 8-mL Percoll solution (225 mM mannitol, 25 mM HEPES [pH 7.4], 1 mM EGTA, 30% Percoll) and topped by 1.5 mL MRB. The Percoll column was centrifuged at 95,000 ×*g* for 30 min at 4 °C. The resulting upper layer, which contained mitochondria-

associated endoplasmic reticulum membranes, and the lower layer, which contained the pure mitochondrial fraction, were gently pipetted and diluted 10 times with MRB. Both fractions were then centrifuged at 6,250 ×*g* for 10 min at 4 °C. The corresponding pellets were discarded, and the supernatants containing mitochondria-associated endoplasmic reticulum membranes were transferred to ultra-clear tubes and ultracentrifuged at 100,000 ×*g* for 1 h (51-Ti rotor, Beckman) at 4 °C. The resulting pellets were snap-frozen and stored at –80 °C until use. For the mitochondrial fractions, the pellets were gently resuspended in 2 mL MRB and centrifuged at 6,250 ×*g* for 10 min at 4 °C. The resulting pellets were snap-frozen and stored at –80 °C until use.

Sub fractionation of skeletal muscle mitochondria

Dissected gastrocnemius and soleus muscles were immediately washed with 2 mL fresh ice-cold MIB buffer (220 mM mannitol, 75 mM sucrose, 10 mM HEPES-KOH [pH 7.4], 10 mM KCl, 1 mM EDTA, 1 mM EGTA, 0.1% BSA, and protease inhibitors). Muscles were cut into small pieces using scalpels, and minced tissues were transferred to a 5-mL glass homogenizer. Ice-cold MIB buffer was added, and the muscles were homogenized using a Teflon pestle (15 strokes). The homogenates were transferred to chilled centrifuge tubes and incubated for 30 min on ice. The samples were centrifuged twice at 700 ×*g* for 5 min at 4 °C. The supernatants were transferred to new tubes and centrifuged at 5,500 ×*g* for 15 min at 4 °C. The pellets were gently resuspended in an equal volume of ice-cold MITO buffer (220 mM mannitol, 75 mM sucrose, 10 mM HEPES-KOH [pH 7.4]). A 20-µL sample of the resuspended pellet suspension was centrifuged at 5,500 ×*g* for 15 min. The resulting mitochondrial pellets were lysed in 20 µL distillated water and then snap frozen. The protein concentrations were determined by OD595 using BSA solution (Pierce). Aliquots (40 µg) of the mitochondrial preparation were placed into six new tubes with a total volume of 100 µL MITO buffer. The following solutions were then added to each tube: 2 µL of 10 mg/mL proteinase K; 700 µL of 20 mM KCl; 700 µL of 20 mM KCl + 8 µL proteinase K; 100 µL of 2% SDS + 2 µL proteinase K; 40 µL of 0.5 µg/µL trypsin. All reactions were incubated for 1 h on

ice and mixed every 10 min. For the alkaline treatment, 10 µL of 1 M sodium bicarbonate was added to the sixth tube; the reaction was incubated for 30 min on ice and mixed every 10 min. After incubation, the samples were centrifuged at 15,000 ×*g* for 15 min, and the pellets were resuspended in 100 µL MITO buffer supplemented with 5 µL of 100% trichloroacetic acid. The samples were incubated at 60 °C for 5 min, cooled on ice for 5 min, and centrifuged at 14,000 rpm at 4 °C for 15 min. The supernatants were aspirated without disturbing the pellets. The pellets were resuspended in 18 µL of 1.5× loading buffer, supplemented with 9 µL of 0.1 M DTT. Samples were run on SDS-polyacrylamide gels and immunoblotted with selected antibodies.

Maintenance of primary myoblast cells in culture

Myoblast cultures were established as described previously[31, 90]. In brief, primary myoblasts from WT, *Alix*$^{-/-}$, and *ccOzz*$^{-/-}$ mice were isolated and maintained on collagen I–coated dishes (BD Biosciences) in Ham's F-10 medium supplemented with 20% fetal calf serum (FCS), 1 ng/mL human basic fibroblast growth factor (Promega), penicillin/streptomycin (Pen/Strep; both at 100 mg/mL) (Gibco-Invitrogen) at 37 °C in 5% CO_2. To differentiate the cells into myotubes, the culture medium was replaced with Dulbecco's Modified Eagle Medium (DMEM) supplemented with L-glutamine and 2% horse serum.

Mitochondrial respiration analysis

Mitochondrial respiration assays were performed using a Seahorse XF96 Cell Mito Stress Test Kit (Agilent-103015-100), in accordance with the manufacturer's instructions. Primary myoblasts were seeded (22,000 cells/well) in triplicates into a collagen I–coated 96-well plate in Ham's F-12 media supplemented with 20% FCS, 1% L-glutamine, 1% Pen/Strep, and 2.5 ng/mL human fibroblast growth factor for 24 h (Day 0). Myoblasts were differentiated for 3 days in DMEM supplemented with 2% horse serum, 1% L-glutamine, and 1% Pen/Strep to form myotubes. One day before analysis, sensor cartridges were hydrated in calibration buffer and placed in a 37 °C

incubator without CO_2. On the day of the experiment, the differentiation medium was changed to Seahorse XF Base Medium (pH 7.4) containing 4 mM glutamine, 5.5 mM glucose, 2 mM pyruvate, and 5 mM HEPES. Myotubes were placed in a 37 °C incubator without CO_2 for 1 h prior to analysis. The OCR, which represents basal respiration, was measured without any additions to the medium. Next, oligomycin was added to inhibit ATP synthase (complex V) and the OCR was recorded. The maximal OCR was measured after the uncoupler FCCP was added, and the nonmitochondrial OCR was measured by adding a mixture of rotenone/antimycin A, which shut down mitochondrial respiration. After the analysis, cells were stained with Hoechst and imaged on an XF96 extracellular flux analyzer (Seahorse Bioscience). OCR results were normalized to nuclei counts and were analyzed using Wave (software for XFp Analyzer, Agilent). Statistical calculations and graphical representations were created using GraphPad software and Microsoft Excel software.

Measurement of mitochondrial membrane potential during myoblast differentiation

WT, *Alix*$^{-/-}$, and *ccOzz*$^{-/-}$ primary myoblasts were seeded (5.0×10^4 cells/well) in triplicates on collagen I–coated 24-well plates and maintained in culture in DMEM supplemented with 20% FCS, 1% L-glutamine, and 1% Pen/Strep at 37 °C/5% CO_2 for 24 h (Day 0). Myoblasts were differentiated for 3 days with DMEM supplemented with 2% horse serum, 1% L-glutamine, and 1% Pen/Strep and maintained in culture at 37 °C/10% CO_2. Prior, to measure the mitochondrial membrane potential ($\Delta\Psi m$), cell was treated for 3 h with 50 μm of MG-132 (Sigma-Millipore). Cells were detached with 0.05% trypsin-EDTA for 5 min at 37 °C and washed twice in 1x PBS. Control and treated cells were incubated at 37 °C for 30 min in media containing TMRE (1 μM) and DAPI (2 μM). Cellular fluorescence was detected by flow cytometry. After measuring the TMRE fluorescence, we treated the cells with FCCP (5 μM final concentration) and incubated them at RT in the dark for 5 min. The dissipation time points of the fluorescence intensity were

analyzed by flow cytometry. The results obtained from the flow cytometer were analyzed using FlowJo software (TreeStar).

Modified Gomori trichrome staining

Consecutive 12-μm sections of unfixed fresh-frozen muscle (WT, *Alix*$^{-/-}$, and *ccOzz*$^{-/-}$) were prepared on a cryostat, stained with Harris' hematoxylin for 5 min, washed with water, and then stained with modified Gomori trichrome stain (0.6 g chromotrope 2R, 0.3 g Fast Green FCF, 0.6 g phosphotungstic acid, 1 mL glacial acetic acid in 100 mL deionized water). The pH was adjusted to 3.4 by using 10 N NaOH for 20 min. The slides were rinsed once in 0.2% acetic acid for 10 s, dehydrated by immersion in ethanol for 2 min (95%, 100%), and cleared twice in xylene by incubating the slides for 3 min. The cross sections were mounted with cytoseal XYL solution. Images were acquired on a Leica microscope using Leica application Suite V4.

Succinate dehydrogenase staining

Cryosections were incubated in SDH-staining buffer (0.2 M phosphate buffer [pH 7.4], 1 mg/mL nitro-blue tetrazolium) at 37 °C for 1 h. The slides were washed thrice with deionized water. Sections were mounted in water-soluble mounting medium. Images were acquired on a Leica microscope using Leica application Suite V4.

Cytochrome C staining

Cryosections were incubated with Cyt C–staining solution (0.2M phosphate buffer [pH 7.4], 0.5 mg/mL DAB, 1 μL/mL of 50 mM catalase solution, 1 mg/mL cyt C type II, 75 mg/mL sucrose) at 37 °C for 3 h. The slides were washed thrice with deionized water and dehydrated in ethanol (50%, 70%, 80%, [2×] 95%, [2×] 100%). The slides were cleared twice in xylene and mounted with cytoseal XYL solution. Images were acquired on a Leica microscope using Leica application Suite V4.

Metabolic profiling analysis of the soleus-extraction of hydrophilic metabolites from skeletal tissues

Soleus muscles were harvested from 8-week-old male mice (Supplementary data 2), rinsed once in ice-cold saline, and gently blotted dry. Tissues were flash-frozen in liquid nitrogen and stored at −80 °C until further processing. To extract metabolites of varying polarity, we employed an adapted three-phase solvent extraction protocol[91]. Briefly, muscle samples were weighed, and 1.2 mL of chloroform:methanol:water (3:4:1, v/v/v) was added. Approximately 25 zirconia beads (1 mm diameter) were added to each tube, and the samples were homogenized at 8 m/s for 30 s using a Bead Ruptor Elite (OMNI International). After homogenization, 150 µL of ice-cold saline was added to promote phase separation, followed by an additional homogenization step. The homogenates were incubated at 4 °C for 30 s and then centrifuged at 21,000 ×g for 10 min at 4 °C. The upper aqueous phase, containing hydrophilic metabolites, was carefully collected, frozen on dry ice, and lyophilized for downstream analyses. Dried hydrophilic metabolite extracts were reconstituted in water:acetonitrile:formic acid (95:5:0.1, v/v/v) at a volume of 5 µL per milligram of tissue processed. Samples were transferred to autosampler vials, and 2 µL of each extract was injected for liquid chromatography–mass spectrometry (LC-MS) analysis. For lipid extraction, the lower organic phase from the initial extraction was transferred to fresh tubes and evaporated to dryness under a gentle stream of nitrogen at room temperature. Dried lipid extracts were reconstituted in chloroform:methanol (2:1, v/v) at a volume of 5 µL per milligram of tissue. Reconstituted samples were transferred to autosampler vials, and 10 µL of each was injected for LC-MS analysis.

LC-MS profiling of hydrophilic metabolites

Liquid chromatography was performed using a Vanquish Horizon UHPLC system (Thermo Fisher Scientific) with the following gradient profile for mobile phase B: 0–16.5 min, 1% to 50%; 16.5–

18 min, 50% to 99%; 18–36 min, 99%; 36–39 min, 99% to 1%; and 39–45 min, 1%. Mobile phase A consisted of water containing 10 mM ammonium formate and 0.1% formic acid; mobile phase B was acetonitrile with 0.1% formic acid. Chromatographic separation was carried out on an Acquity UPLC BEH Amide column (1 × 150 mm, 1.7 µm; Waters Corp.), maintained at 40 °C. The flow rate was set to 50 µL/min, and the injection volume was 2 µL.

Mass spectrometry was performed on a Q Exactive Hybrid Quadrupole-Orbitrap mass spectrometer (Thermo Fisher Scientific) equipped with a HESI-II electrospray ionization (ESI) source. Samples were analyzed in both positive and negative ionization modes, using separate chromatographic runs for each polarity. The instrument operated in data-dependent acquisition (DDA) mode, selecting the top 10 most abundant precursor ions for MS/MS fragmentation (Top10 dd-MS^2). Full MS (MS^1) scans were acquired at a resolution of 140,000 (FWHM at *m/z* 200), with an automatic gain control (AGC) target of 3×10^6 and a maximum injection time of 100 ms. The scan range was set to *m/z* 60–900. For MS^2 scans, a resolution of 35,000 was used, with an AGC target of 1×10^5, a maximum injection time of 60 ms, and an isolation window of 1.0 *m/z*. Fragmentation was achieved using higher-energy collisional dissociation (HCD) with a normalized collision energy (NCE) of 35. Ion source parameters were as follows: sheath gas flow rate, 20; auxiliary gas flow rate, 5; sweep gas flow rate, 1. The spray voltage was set to 3.6 kV in positive mode and 2.5 kV in negative mode. The capillary temperature and auxiliary gas heater temperature were both maintained at 320 °C. The S-lens RF level was set to 55.

Data processing, metabolite identification, and statistics

Untargeted metabolomic analyses were processed using Compound Discoverer 3.3 (CD3.3, Thermo Fisher Scientific) and MetaboAnalyst 6.0. For CD3.3, we employed the predefined "Untargeted Metabolomics with Statistics" workflow. This pipeline detects unknown compounds using online databases and maps identified metabolites to biological pathways via the Metabolika software. Spectral alignment was performed using the adaptive curve algorithm with a maximum

retention time (RT) shift of 2 minutes. Compound detection settings included a signal-to-noise ratio (S/N) ≥ 2, a minimum peak intensity of 1×10^6, a parent ion mass tolerance of ±5 ppm, RT tolerance of 0.25 min, and preferred fragment ion selection of M+H and M–H. Data normalization was conducted using the constant mean algorithm. Metabolite identification and pathway mapping were conducted using default settings in the CD3.3 workflow. Compound Discoverer provided both raw and adjusted p-values in the results tables. Although volcano plots generated by CD3.3 display raw p-values by default, all downstream statistical analyses and feature selection were performed using MetaboAnalyst 6.0. MetaboAnalyst applies false discovery rate (FDR) correction (default threshold: 0.05) across its modules, ensuring robust control for multiple comparisons. Consequently, all reported statistical interpretations and metabolite selections were based on FDR-adjusted p-values. Data tables exported from CD3.3 were formatted in Microsoft Excel and imported into MetaboAnalyst 6.0 for multivariate statistical analysis, metabolite set enrichment analysis (MSEA), and metabolic pathway analysis. Data are expressed as mean ± standard error of the mean (SEM). Statistical differences between treated and control groups were evaluated using CD3.1, LipidSearch v4.1, and MetaboAnalyst 6.0. Differences were considered statistically significant at $p \leq 0.05$; non-significant results are denoted as "NS." Graphical representations were created using Adobe Illustrator.

Extraction of metabolites for targeted analysis of Tricarboxylic acid (TCA) cycle intermediates

Soleus muscles of 8-week-old males and female mice were collected and flash-frozen in liquid nitrogen and stored at −80 °C. To extract the molecules of interest we adapted a procedure to separate the hydrophilic metabolites from lipids, then they were derivatized by silylation and then analyze the by GC-MS[92]. Briefly, the whole frozen soleus muscle was accurately weighed and then 1 mL of methanol/water (1:1, v/v) was added onto the frozen tissue sample and then homogenized after adding approx. 25 1-mm zirconia beads using a Bead Ruptor Elite (OMNI

international, Kennesaw GA, USA) for 30 sec at 8 m/s. Next, 400 µL of chloroform was added and the tubes were briefly mixed again in the Bead Ruptor. The homogenate was allowed to rest at 4 ºC for 30 sec and centrifuged for 10 min at 21,000 g at 4 ºC. After centrifugation, the upper aqueous phases were transferred into new glass tubes and evaporated to dryness under a steam of nitrogen at RT. The dried residues were dissolved in 25 µl of methoxylamine solution (2% MOX in pyridine) (Sigma-Aldrich, St. Louis, MO, USA) and incubated at 37 ºC for 2 h in the tightly capped glass tubes. Next, the samples were derivatized with 50 µl of MTBSTFA + 1% t-BDMCS (Sigma-Aldrich) and incubated for 1 h at 60 ºC. The silylated samples were transferred into autosampler vials and 1 µl was analyzed by GC-MS.

GC-MS determination of the TCA metabolites

Silylated derivatives were separated in a VF5ms capillary column (60 m +10m guard × 0.25 mm, 0.25 µm; Agilent Technologies, Santa Clara, CA, USA), using an Agilent 7890B GC system and the following gradient conditions: 0-1 min 80 ºC; 1-25 min 80-to-250 ºC; 25-26 min 250-to-300 ºC; 26-40 min 300 ºC. The carrier gas was ultrapure helium (1.0 ml/min). Analytical determinations were performed with an Agilent 5977B mass-selective detector (MSD) with a front inlet temperature of 250 ºC operating in no-split mode, the GC-MSD interface temperature was 300 ºC and the ion source and quadrupole temperatures were both 150 ºC. The MSD had an electron impact (EI) ion source operated at 70 eV, and we used the SIM mode to acquire quantitative data from all the targeted analytes.

SIM-parameters of TCA analytes

The Selected Ion Monitoring (SIM) were established using commercially available standards (Sigma-Aldrich) for all analytes and the resulting conditions were used for the quantitative determination of the TCA intermediates in the tissue samples.

Analyte/RT window	m/z Fragments record	Dwell time (ms)
Succinate 23:0–24:6 min	m/z 116 m/z 215 m/z 289 (quantification ion) m/z 331	20 20 60 20
Fumarate 24:6–26:0 min	m/z 230 m/z 245 m/z 287 (quantification ion) m/z 329	20 20 60 20
α-Ketoglutarate 27:0–28:0 min	m/z 156 m/z 258 m/z 346 (quantification ion) m/z 388	20 20 60 20
Malate 28:0–28:9 min	m/z 287 m/z 403 m/z 419 (quantification ion)	20 20 60
Citrate/Isocitrate 32:4–40:0 min	m/z 259 m/z 357 m/z 431 m/z 459 (quantification ion)	20 20 20 60

Data processing and statistics

GMS data were acquired and processed using the MassHunter B.07 software (Agilent Technologies). For every analyte, only the quantification ion was tabulated and used for graphs and statistical analyses performed using Excel. Data represents the means ± standard error of the mean of the metabolite's peak area, Student's t-Test (1-tailed, homoscedastic), considering significant differences for p-values ≤0.05; NS denotes non-significant differences. A graphical representation was generated using Adobe Illustrator software.

Glycolytic Rate Assay

Glycolysis was assessed using the Seahorse XF Glycolytic Rate Assay Kit (Agilen-103344-100), following the manufacturer's guidelines. Briefly, cells were prepared and seeded similarly to those in the mitochondrial respiration assays. On the day of experimentation, the differentiation medium was replaced with Seahorse XF Base Medium (pH 7.4), supplemented with 4 mM glutamine, 5.5 mM glucose, and 2 mM pyruvate. Myotubes were then incubated at 37°C without CO2 for 1 hour

prior to analysis. Basal respiration (OCR) and glycolysis (ECAR) were measured without any additional medium components. Subsequently, a mixture of rotenone and antimycin A was injected to assess compensatory glycolysis levels. Glycolysis inhibition was evaluated following the addition of 2-deoxy-D-glucose (2-DG). The resultant decrease in Proton Efflux Rate (PER) served as qualitative confirmation that the PER observed prior to 2-DG administration primarily resulted from glycolysis. Following analysis, cells were imaged using an XF96 extracellular flux analyzer from Seahorse Bioscience. Glycolytic rate data were normalized to cell counts and analyzed using Wave software (Agilent). Statistical analysis and graphical representations were generated using GraphPad and Adobe Illustrator software.

Mitochondrial and nuclear DNA copy number assays

Soleus muscles were collected from WT, *Alix*$^{-/-}$, and *ccOzz*$^{-/-}$ mice. Total genomic DNA was extracted from the muscles using the QIAamp DNA Mini Kit (Qiagen), following the manufacturer's guidelines. DNA quantity and purity were measured using Qubit 4 Fluorometer (Thermo Scientific). Quantitative polymerase chain reaction (qPCR) was performed using SsoAdvanced universal SYBR green supermix (Bio Rad), 5 ng genomic DNA, 10 µM primers (mMitoF1: 5' CTA GAA ACC CCG AAA CCA AA 3', mMitoR1: 5' CCA GCT ATC ACC AAG CTC GT 3', mB2MF1: 5'ATG GGA AGC CGA ACA TAC TG 3' and mB2MR1: 5' CAG TCT CAG TGG GGG TGA AT 3' [3, 93]and RNAse free water in a 25 µL reaction volume on a CFX96 opus 96 Real-Time PCR system (Bio-Rad). The copy number was calculated using the molecular weight of PCL20C plasmid. The standard curve was generated for quantification of the viral genome using the following primers: pcL20-pack-For: 5' CTC TCT CGA CGC AGG ACT CG 3', pcL20-pack-Rev: 5' GAC GCT CTC GCA CCC ATC T 3'. pcL20c standard curve: $1.04x10^2$, $1.04x10^3$, $1.04x10^4$, $1.04x10^5$, $1.04x10^6$, $1.04x10^7$, $1.04x10^8$, $1.04x10^9$, and $1.04x10^{10}$ copies of plasmid DNA. All samples were tested in triplicate and a "no template DNA/H_2O" negative control (H_2O) was included to monitor sample

contamination. The qPCR cycles were as follows: 1. 50°C for 2:00, 2. 95°C for 2:00, 3. 95°C for 0:15, 4. 60°C for 1:00, 5. Repeat 3–4 39x.

Immunofluorescence and imaging

Cross sections of soleus muscle were fixed and permeabilized with 1% PFA, 0.4% Triton-X 100 in 1× PBS for 15 min at RT. Sections were blocked for 1 h in blocking buffer (PBS containing 5% normal donkey serum, 0.1% BSA, and 0.4% Triton X-100) and then incubated with myosin antibodies (Antibodies and reagents) diluted in blocking buffer at 4 °C overnight. Next day, the slides were washed thrice with washing buffer (PBS containing 0.4% Triton X-100) and incubated with secondary antibody diluted in blocking buffer at 4 °C for 1 h. Following three washings, the sections were mounted with ProLong Gold antifade reagent with DAPI. Images were acquired on a Nikon C2 confocal microscope using NIS Elements software. Images were segmented by fluorescence using an ilastik pixel classifier. Fluorescent cross-sectioned images of the soleus were segmented by myosin fiber types (slow MyHC or MyHC IIA) using a pixel classifier developed in ilastik. Segmented images were analyzed using a macro developed in FIJI to quantify the number of each type of fiber using the analyze particle's function. Percentages of each fiber type we calculated based on the total number of fibers. Statistical analysis and graphical representations were generated using GraphPad and Adobe Illustrator software.

Determination of ATPase activity

Frozen serial sections of the soleus were air dried at RT for 5 min. Slides were incubated in acid preincubation buffer (50 mM potassium acetate, 17.7 mM $CaCl_2$ dihydrate [pH 4.5], with glacial acetic acid and filtered at 0.22 µm) at RT for 2 min and washed thrice with Tris-buffer (100 mM Tris base, 17.7 mM $CaCl_2$ dihydrate [pH 7.8], with 5 N HCl and filtered at 0.22 µm) for 2 min. The slides were transferred to a container with basic incubation buffer (20 mM KCl, 2.7 mM ATP, disodium salt, 50 mM $CaCl_2$ dihydrate, 100 mM 2-amino-2-methyl-propanol HCl [pH 10.5], with 1

N HCl, not filtered) and incubated at 24 °C for 25 min. The slides were rinsed four times in three changes of 1% $CaCl_2$ and stained in 0.1% toluidine blue for 45 s. The slides were rinsed in distilled H_2O for 30 s and dehydrated by dipping five times in serial concentrations of ethanol (95%, 100%, 100%). The slides were cleared twice in xylene for 3 min and mounted with cytoseal XYL. Images were acquired on a AxioScan Z.1 Whole Slide Scanner using Zen Black (Zeiss) software. A macro was developed in FIJI to count the different types of myosin fibers (Type I, IIA, IIX) in the soleus. The macro included a threshold for detection for each fiber type to quantify the number of fibers per field of view using the analyze particle's function. Statistical analysis and graphical representations were generated using GraphPad and Adobe Illustrator software.

Generation, transduction, and purification of biotinylated Ozz

The biotinylating procedure was performed as described previously[58, 59]. *Ozz* cDNA was cloned in the pBABE-puro vector containing the 23–amino acid biotinylation tag (Avi-tag). Retrovirus particles were produced by transfecting the packaging cell line Eco Phoenix with Avi-pBABE-puro or Avi-Ozz-pBABE-puro plasmids using the transfection reagent FuGENE 6. BirA-C2C12 cells, generously provided by G. Grosveld of St. Jude Children's Research Hospital, were transduced with Avi-pBABE-puro or Avi-Ozz-pBABE-puro retroviruses for 48 h, followed by neomycin (0.8 mg/mL) and puromycin (3 μg/mL) selection for 5 days. Selected cells were maintained in DMEM plus medium (DMEM supplemented with 20% FCS, L-glutamine, 10^4 U/mL/10^4 μg/mL penicillin/streptomycin, 0.8 mg/mL neomycin, and 1.0 μg/mL puromycin). For purification of biotinylated proteins, 1.0×10^6 C2C12 cells were seeded in 150 cm^2 flasks and grown in DMEM plus medium containing 50mM of biotin (Day 0). For differentiated C2C12 cells, 3.0×10^6 C2C12 cells were seeded in 150 cm^2 flasks and grown in DMEM plus medium, which was changed after 48 h for DMEM medium supplemented with 2% horse serum, L-glutamine, 10^4 U/mL/10^4 μg/mL penicillin/streptomycin, 0.8 mg/mL neomycin, 1.0 μg/mL puromycin, and 50 mM of biotin and incubated for 72 h. (Day 3). All cell cultures were grown at 37 °C in 5% CO_2. Cell pellets were

collected from Avi-Ozz–overexpressing C2C12 cells at Day 0 and Day 3. For crude mitochondria preparations, the same overexpressing cells were first lysed in ice-cold lysis buffer (1× TBS [pH 8.0], 0.3% NP-40, 20% glycerol, 0.215 mM EDTA [pH 8.0], 150 mM KCl, CelLytic Express, protease inhibitors, and phosphatase inhibitors) by using a Dounce homogenizer (15 strokes). The homogenates were kept on ice with slight agitation for 30 min and centrifuged at 16,000 ×*g* for 10 min at 4 °C. The resulting supernatants were transferred into fresh tubes, and protein concentrations were measured. Paramagnetic streptavidin beads were blocked by washing them thrice in 1× TBS with 200 ng/μL purified chicken serum albumin (Sigma-Aldrich). Approximately 20 μL of beads were added per 1 mg of soluble extract. Binding of the samples to the beads was done in a solution of 1× TBS (pH 8.0), 0.3% NP-40, 20% glycerol, 0.215 mM EDTA (pH 8.0), 150mM KCl, at 4 °C under agitation from 1 h to overnight. The samples were washed six times in binding solution at RT. Bound proteins were released by boiling the beads in sample buffer and then identified by SDS-PAGE under denaturing conditions and immunoblotting with selected antibodies.

Generation, transduction, and purification of FLAG-Alix

C2C12 (ATCC, CRL-1772) cells were transduced with MSCV-GFP empty vector or MSCV-GFP expressing N-terminal FLAG-tagged full-length Alix. At 72 h after transduction, cells were sorted and selected by GFP expression. A total of 1.0 × 10^6 C2C12 cells were seeded into 150 cm^2 flasks. Proliferating cells were grown in DMEM supplemented with 20% FCS, L-glutamine, 10^4 U/mL/10^4 μg/mL penicillin/streptomycin and differentiated C2C12 cells were grown in DMEM supplemented with 2% horse serum, L-glutamine, and 10^4 U/mL//10^4 μg/mL penicillin/streptomycin. Cells were grown at 37 °C in 5% CO_2. Mitochondrial preparations from C2C12 cells overexpressing FLAG-tagged full-length Alix were lysed with ice-cold lysis buffer (1× TBS [pH 8.0], 0.3% NP-40, 20% glycerol, 0.215 mM EDTA [pH 8.0], 150 mM KCl, protease inhibitors, and phosphatase inhibitors) by using a Dounce homogenizer (15 strokes). The

homogenates were kept on ice with slight agitation for 30 min and centrifuged at 20,000 rpm for 10 min. The resulting supernatants were transferred into clean tubes and protein concentration was measured. Samples were applied to pre-equilibrated anti-FLAG M2 affinity gel and incubated at 4 °C for 1 h. The incubated resin was collected by centrifugation at 1,500 rpm for 5 min at 4 °C and washed with lysis buffer. After extensive washing, the FLAG-tagged protein was eluted using 3× FLAG peptide (St. Jude Peptide Synthesis Facility), and eluted fractions were subjected to SDS–PAGE under denaturing conditions followed by immunoblotting with the indicated antibodies.

Coimmunoprecipitations

For immunoprecipitation experiments, crude mitochondria preparations were lysed with 1× TEVP buffer[94] (10 mM Tris base, 5 mM NaF, 1 mM Na_3VO_4, 1 mM EDTA, 1 mM EGTA [pH 7.4]) supplemented with 0.5% Triton X-100 and protease inhibitors. Mitochondrial lysates (140 µg) were incubated with anti-SLC25A4 antibody (5 µg) at 4 °C overnight. Samples were immunoprecipitated with 40 µL Pure Proteome Protein A/G Mix Magnetic Beads coupled to V5 peptide at 4 °C for 1 h. The beads were washed thrice with ice-cold lysis buffer and once with 1× TEVP buffer. Bound proteins were released by boiling the beads in sample buffer. They were then run on SDS-polyacrylamide gels, under denaturing conditions, followed by immunoblotting with the indicated antibodies.

In vitro ubiquitination of mitochondria proteins

The ubiquitination assay was performed by incubating 1.0 µM of a bacterially expressed GST-SLC25A4 with 100 nM purified recombinant E1, 1µM purified recombinant E2, 1.0 µM $CRL5^{Ozz}$ ubiquitin ligase, and 50 µM ubiquitin in a final volume of 20 µL 1X ubiquitination buffer and 1X ATP at 37 °C for 2 h[95]. To analyze the ubiquitinated products, we diluted the ubiquitination reaction

in 2X of loading buffer (Bio Rad) and boiled at 95C for 5 min. The samples were resolved on 10% SDS-PAGE and immunoblotted with anti-ubiquitin, anti-SLc25A4 or anti-GST antibodies.

To denature GST-Slc25A4, 9 μg of the protein was heat at 55 °C for 5 min. After the denaturation step, the samples were centrifuge at 12000 rpm for 5 min. The supernatant was transfer to a fresh tube and quantified. For the ubiquitination reaction, we used ~1.0 μM of denature GST-Slc25A4.

Exosome isolation from skeletal muscle

Exosomes were isolated as described previously[60]. Briefly, gastrocnemius or soleus muscles of 8-week-old mice were collected and washed once with ice-cold 1× PBS. Tissues were gently sliced into small fragments and transferred to glass homogenization tubes containing 4 mL ice-cold 1× PBS. The samples were hand homogenized at 8,000 rpm (20 strokes) and transferred to 5-mL centrifuge tubes. Exosomes were purified by sequential centrifugation steps at 300 ×*g* for 10 min, 2000 ×*g* for 10 min, and 10,000 ×*g* for 30 min to remove cells and cell debris. The supernatants were then ultracentrifuged at 100,000 ×*g* for 120 min at 4 °C. The supernatant was discarded, and the exosome pellets were washed once with cold PBS and then ultracentrifuged at 100,000 ×*g* at 4 °C for 2 h. Exosomal pellets were resuspended in 0.25 M sucrose and loaded onto a step gradient of 2 to 0.5 M sucrose in 10 mM tris-HCl buffer (pH 7.4) and 1 mM Mg $(Ac)_2$. The gradients were ultracentrifuged at 100,000 ×*g* for 2.5 h in a Beckman Coulter SW41Ti rotor. Fractions were collected and precipitated with 100% trichloroacetic acid (110 μL). Pellets were resuspended in NuPAGE lithium dodecyl sulfate sample buffer (Life Technologies or Bio-Rad) with or without DTT and used for Western blot analyses. After isolation of exosomes, the muscle homogenized were subject to sub-fractionation similar to the method describe in Sub fractionation of skeletal muscle mitochondria.

Mito-QC mouse model

The mito-QC mouse model was generated as previously described by McWilliams et al., 2016[51]. To quantify mitochondria undergoing mitophagy (red-only puncta) in the soleus muscle of mitoQC/WT, mitoQC/*Alix*$^{-/-}$ and mitoQC/*ccOzz*$^{-/-}$, we developed a macro in FIJI to calculate the number of red-only puncta by setting a threshold of detection and using the analyze particle's function. Total fiber area was quantified using a lower threshold to detect all stained tissue. The percent of red-only puncta was quantified per area of fiber. Statistical analysis and graphical representations were generated using GraphPad and Adobe Illustrator software.

Statistics and reproducibility

To ensure data reproducibility, all experiments were performed in biological replicates (two or three, as indicated). Sample sizes and the number of replicates are provided in the Supplementary data, which also specify how replicates were defined.

Data were expressed as mean ± standard deviation[76] and evaluated using Student's *t*-test or Ordinary one-way ANOVA test for comparison with WT samples. Mean differences were considered statistically significant when P-values were less than 0.05.

Statistical analyses were performed using GraphPad Prism. Quantitative data are presented as median ± quartiles, or as mean ± S.D. For comparisons between 2 groups, Student's t-tests (paired or unpaired, 2-tailed) were performed. For small sample sizes (n <6), a Welch's correction was applied to the student's t-test. For comparisons of 3 or more groups, one-way or two-way ANOVAs were performed. Significance was defined as $p < 0.05$.

Data availability

All data supporting the findings of this study are available in the article and its supplementary information. Additional information can be obtained from the corresponding authors upon request. Metabolomics data have been uploaded to Metabolomics Workbench; the accession number

is: **ST004190**. All numerical source data underlying Figs. 3–6 and Supplementary Figs. S3, S4, S6, and S7, together with the complete metabolomic dataset, are supplied in the Supplementary Data. Uncropped blot and gel images can be found in the Supplementary Information.

REFERENCES

1. Mukund, K. & Subramaniam, S. Skeletal muscle: A review of molecular structure and function, in health and disease. *Wiley Interdiscip Rev Syst Biol Med* **12**, e1462 (2020).
2. Schiaffino, S. & Reggiani, C. Fiber types in mammalian skeletal muscles. *Physiol Rev* **91**, 1447-1531 (2011).
3. Ortenblad, N. *et al.* The Muscle Fiber Profiles, Mitochondrial Content, and Enzyme Activities of the Exceptionally Well-Trained Arm and Leg Muscles of Elite Cross-Country Skiers. *Front Physiol* **9**, 1031 (2018).
4. A. Damirchi, P.B., M. Gholamali, K. Ranjbar Mitochondrial Biogenesis in Skeletal Muscle: Exercise and Aging, in *Skeletal Muscle - From Myogenesis to Clinical Relations* (IntechOpen, 2012).
5. Hood, D.A., Memme, J.M., Oliveira, A.N. & Triolo, M. Maintenance of Skeletal Muscle Mitochondria in Health, Exercise, and Aging. *Annu Rev Physiol* **81**, 19-41 (2019).
6. Mishra, P., Varuzhanyan, G., Pham, A.H. & Chan, D.C. Mitochondrial Dynamics is a Distinguishing Feature of Skeletal Muscle Fiber Types and Regulates Organellar Compartmentalization. *Cell Metab* **22**, 1033-1044 (2015).
7. Krylova, S.V. & Feng, D. The Machinery of Exosomes: Biogenesis, Release, and Uptake. *Int J Mol Sci* **24** (2023).
8. Picca, A. *et al.* Mitochondrial-derived vesicles in skeletal muscle remodeling and adaptation. *Semin Cell Dev Biol* **143**, 37-45 (2023).
9. Romanello, V. The Interplay between Mitochondrial Morphology and Myomitokines in Aging Sarcopenia. *Int J Mol Sci* **22** (2020).
10. Ahmed, S.T., Craven, L., Russell, O.M., Turnbull, D.M. & Vincent, A.E. Diagnosis and Treatment of Mitochondrial Myopathies. *Neurotherapeutics* **15**, 943-953 (2018).
11. Brunel-Guitton, C., Levtova, A. & Sasarman, F. Mitochondrial Diseases and Cardiomyopathies. *Can J Cardiol* **31**, 1360-1376 (2015).
12. Gehrig, S.M. *et al.* Altered skeletal muscle (mitochondrial) properties in patients with mitochondrial DNA single deletion myopathy. *Orphanet J Rare Dis* **11**, 105 (2016).
13. Bragoszewski, P., Turek, M. & Chacinska, A. Control of mitochondrial biogenesis and function by the ubiquitin-proteasome system. *Open Biol* **7** (2017).
14. Lehmann, G., Udasin, R.G. & Ciechanover, A. On the linkage between the ubiquitin-proteasome system and the mitochondria. *Biochem Biophys Res Commun* **473**, 80-86 (2016).
15. Jeon, H.B. *et al.* A proteomics approach to identify the ubiquitinated proteins in mouse heart. *Biochem Biophys Res Commun* **357**, 731-736 (2007).
16. Lavie, J. *et al.* Ubiquitin-Dependent Degradation of Mitochondrial Proteins Regulates Energy Metabolism. *Cell Rep* **23**, 2852-2863 (2018).
17. Alsayyah, C., Ozturk, O., Cavellini, L., Belgareh-Touze, N. & Cohen, M.M. The regulation of mitochondrial homeostasis by the ubiquitin proteasome system. *Biochim Biophys Acta Bioenerg* **1861**, 148302 (2020).
18. Dimmer, K.S. & Scorrano, L. (De)constructing mitochondria: what for? *Physiology (Bethesda)* **21**, 233-241 (2006).
19. Soubannier, V. *et al.* A vesicular transport pathway shuttles cargo from mitochondria to lysosomes. *Curr Biol* **22**, 135-141 (2012).
20. Boudreau, L.H. *et al.* Platelets release mitochondria serving as substrate for bactericidal group IIA-secreted phospholipase A2 to promote inflammation. *Blood* **124**, 2173-2183 (2014).
21. Mathivanan, S., Fahner, C.J., Reid, G.E. & Simpson, R.J. ExoCarta 2012: database of exosomal proteins, RNA and lipids. *Nucleic Acids Res* **40**, D1241-1244 (2012).
22. Ng, M.Y.W., Wai, T. & Simonsen, A. Quality control of the mitochondrion. *Dev Cell* **56**, 881-905 (2021).
23. Puhm, F. *et al.* Mitochondria Are a Subset of Extracellular Vesicles Released by Activated Monocytes and Induce Type I IFN and TNF Responses in Endothelial Cells. *Circ Res* **125**, 43-52 (2019).
24. Ashrafi, G. & Schwarz, T.L. The pathways of mitophagy for quality control and clearance of mitochondria. *Cell Death Differ* **20**, 31-42 (2013).
25. Chen, C.C.W., Erlich, A.T., Crilly, M.J. & Hood, D.A. Parkin is required for exercise-induced mitophagy in muscle: impact of aging. *Am J Physiol Endocrinol Metab* **315**, E404-E415 (2018).

26. Ma, K. *et al.* Mitophagy, Mitochondrial Homeostasis, and Cell Fate. *Front Cell Dev Biol* **8**, 467 (2020).
27. Pickles, S., Vigie, P. & Youle, R.J. Mitophagy and Quality Control Mechanisms in Mitochondrial Maintenance. *Curr Biol* **28**, R170-R185 (2018).
28. Romanello, V. & Sandri, M. Mitochondrial Quality Control and Muscle Mass Maintenance. *Front Physiol* **6**, 422 (2015).
29. Song, J., Herrmann, J.M. & Becker, T. Quality control of the mitochondrial proteome. *Nat Rev Mol Cell Biol* **22**, 54-70 (2021).
30. Campos, Y. *et al.* Biophysical and functional study of CRL5(Ozz), a muscle specific ubiquitin ligase complex. *Sci Rep* **12**, 7820 (2022).
31. Nastasi, T. *et al.* Ozz-E3, a muscle-specific ubiquitin ligase, regulates beta-catenin degradation during myogenesis. *Dev Cell* **6**, 269-282 (2004).
32. Lee, J. *et al.* Neur1 and Neur2 are required for hippocampus-dependent spatial memory and synaptic plasticity. *Hippocampus* **30**, 1158-1166 (2020).
33. Liu, S. & Boulianne, G.L. The NHR domains of Neuralized and related proteins: Beyond Notch signalling. *Cell Signal* **29**, 62-68 (2017).
34. Campos, Y. *et al.* Ozz-E3 ubiquitin ligase targets sarcomeric embryonic myosin heavy chain during muscle development. *PloS one* **5**, e9866 (2010).
35. Bongiovanni, A. *et al.* Alix protein is substrate of Ozz-E3 ligase and modulates actin remodeling in skeletal muscle. *The Journal of biological chemistry* **287**, 12159-12171 (2012).
36. Cabezas, A., Bache, K.G., Brech, A. & Stenmark, H. Alix regulates cortical actin and the spatial distribution of endosomes. *J Cell Sci* **118**, 2625-2635 (2005).
37. Campos, Y. *et al.* Alix-mediated assembly of the actomyosin-tight junction polarity complex preserves epithelial polarity and epithelial barrier. *Nat Commun* **7**, 11876 (2016).
38. Carlton, J.G. & Martin-Serrano, J. Parallels between cytokinesis and retroviral budding: a role for the ESCRT machinery. *Science* **316**, 1908-1912 (2007).
39. Katzmann, D.J., Odorizzi, G. & Emr, S.D. Receptor downregulation and multivesicular-body sorting. *Nat Rev Mol Cell Biol* **3**, 893-905 (2002).
40. Martin-Serrano, J., Yarovoy, A., Perez-Caballero, D. & Bieniasz, P.D. Divergent retroviral late-budding domains recruit vacuolar protein sorting factors by using alternative adaptor proteins. *Proc Natl Acad Sci U S A* **100**, 12414-12419 (2003).
41. Morita, E. *et al.* Human ESCRT and ALIX proteins interact with proteins of the midbody and function in cytokinesis. *EMBO J* **26**, 4215-4227 (2007).
42. Pan, S. *et al.* Involvement of the conserved adaptor protein Alix in actin cytoskeleton assembly. *The Journal of biological chemistry* **281**, 34640-34650 (2006).
43. Raiborg, C., Rusten, T.E. & Stenmark, H. Protein sorting into multivesicular endosomes. *Curr Opin Cell Biol* **15**, 446-455 (2003).
44. Schmidt, M.H.H., Chen, B., Randazzo, L.M. & Bogler, O. SETA/CIN85/Ruk and its binding partner AIP1 associate with diverse cytoskeletal elements, including FAKs, and modulate cell adhesion. *J Cell Sci* **116**, 2845-2855 (2003).
45. Strack, B., Calistri, A., Craig, S., Popova, E. & Gottlinger, H.G. AIP1/ALIX is a binding partner for HIV-1 p6 and EIAV p9 functioning in virus budding. *Cell* **114**, 689-699 (2003).
46. Sun, S. *et al.* ALG-2 activates the MVB sorting function of ALIX through relieving its intramolecular interaction. *Cell Discov* **1**, 15018 (2015).
47. Romancino, D.P. *et al.* Identification and characterization of the nano-sized vesicles released by muscle cells. *FEBS Lett* **587**, 1379-1384 (2013).
48. Drake, J.C. & Yan, Z. Mitophagy in maintaining skeletal muscle mitochondrial proteostasis and metabolic health with ageing. *J Physiol* **595**, 6391-6399 (2017).
49. Guan, Y., Drake, J.C. & Yan, Z. Exercise-Induced Mitophagy in Skeletal Muscle and Heart. *Exerc Sport Sci Rev* **47**, 151-156 (2019).
50. Leduc-Gaudet, J.P., Hussain, S.N.A., Barreiro, E. & Gouspillou, G. Mitochondrial Dynamics and Mitophagy in Skeletal Muscle Health and Aging. *Int J Mol Sci* **22** (2021).
51. McWilliams, T.G. *et al.* mito-QC illuminates mitophagy and mitochondrial architecture in vivo. *J Cell Biol* **214**, 333-345 (2016).
52. Gutierrez-Aguilar, M. & Baines, C.P. Physiological and pathological roles of mitochondrial SLC25 carriers. *Biochem J* **454**, 371-386 (2013).

53. Kunji, E.R.S., King, M.S., Ruprecht, J.J. & Thangaratnarajah, C. The SLC25 Carrier Family: Important Transport Proteins in Mitochondrial Physiology and Pathology. *Physiology (Bethesda)* **35**, 302-327 (2020).
54. Palmieri, F. Mitochondrial transporters of the SLC25 family and associated diseases: a review. *J Inherit Metab Dis* **37**, 565-575 (2014).
55. Ruprecht, J.J. & Kunji, E.R.S. The SLC25 Mitochondrial Carrier Family: Structure and Mechanism. *Trends Biochem Sci* **45**, 244-258 (2020).
56. Chandel, N.S. Glycolysis. *Cold Spring Harb Perspect Biol* **13** (2021).
57. Moreno-Justicia, R. *et al.* Human skeletal muscle fiber heterogeneity beyond myosin heavy chains. *Nat Commun* **16**, 1764 (2025).
58. de Boer, E. *et al.* Efficient biotinylation and single-step purification of tagged transcription factors in mammalian cells and transgenic mice. *Proc Natl Acad Sci U S A* **100**, 7480-7485 (2003).
59. Driegen, S. *et al.* A generic tool for biotinylation of tagged proteins in transgenic mice. *Transgenic Res* **14**, 477-482 (2005).
60. van de Vlekkert, D. *et al.* Excessive exosome release is the pathogenic pathway linking a lysosomal deficiency to generalized fibrosis. *Sci Adv* **5**, eaav3270 (2019).
61. Jezek, P., Jaburek, M., Holendova, B., Engstova, H. & Dlaskova, A. Mitochondrial Cristae Morphology Reflecting Metabolism, Superoxide Formation, Redox Homeostasis, and Pathology. *Antioxid Redox Signal* **39**, 635-683 (2023).
62. Joubert, F. & Puff, N. Mitochondrial Cristae Architecture and Functions: Lessons from Minimal Model Systems. *Membranes (Basel)* **11** (2021).
63. Patten, D.A. *et al.* OPA1-dependent cristae modulation is essential for cellular adaptation to metabolic demand. *EMBO J* **33**, 2676-2691 (2014).
64. Nederveen, J.P. *et al.* Variability in skeletal muscle fibre characteristics during repeated muscle biopsy sampling in human vastus lateralis. *Appl Physiol Nutr Metab* **45**, 368-375 (2020).
65. Van de Casteele, F. *et al.* Does one biopsy cut it? Revisiting human muscle fiber type composition variability using repeated biopsies in the vastus lateralis and gastrocnemius medialis. *J Appl Physiol (1985)* **137**, 1341-1353 (2024).
66. Liu, J. *et al.* Coupling of mitochondrial function and skeletal muscle fiber type by a miR-499/Fnip1/AMPK circuit. *EMBO Mol Med* **8**, 1212-1228 (2016).
67. Coyne, L.P. & Chen, X.J. Consequences of inner mitochondrial membrane protein misfolding. *Mitochondrion* **49**, 46-55 (2019).
68. Gariballa, N. & Ali, B.R. Endoplasmic Reticulum Associated Protein Degradation (ERAD) in the Pathology of Diseases Related to TGFbeta Signaling Pathway: Future Therapeutic Perspectives. *Front Mol Biosci* **7**, 575608 (2020).
69. Olzmann, J.A., Kopito, R.R. & Christianson, J.C. The mammalian endoplasmic reticulum-associated degradation system. *Cold Spring Harb Perspect Biol* **5** (2013).
70. Azzu, V. & Brand, M.D. Degradation of an intramitochondrial protein by the cytosolic proteasome. *J Cell Sci* **123**, 578-585 (2010).
71. Azzu, V., Mookerjee, S.A. & Brand, M.D. Rapid turnover of mitochondrial uncoupling protein 3. *Biochem J* **426**, 13-17 (2010).
72. Mookerjee, S.A. & Brand, M.D. Characteristics of the turnover of uncoupling protein 3 by the ubiquitin proteasome system in isolated mitochondria. *Biochim Biophys Acta* **1807**, 1474-1481 (2011).
73. Klingenberg, M. The ADP and ATP transport in mitochondria and its carrier. *Biochim Biophys Acta* **1778**, 1978-2021 (2008).
74. Hers, H.G. & Van Schaftingen, E. Fructose 2,6-bisphosphate 2 years after its discovery. *Biochem J* **206**, 1-12 (1982).
75. Maldonado, E.N. & Lemasters, J.J. ATP/ADP ratio, the missed connection between mitochondria and the Warburg effect. *Mitochondrion* **19 Pt A**, 78-84 (2014).
76. Mor, I., Cheung, E.C. & Vousden, K.H. Control of glycolysis through regulation of PFK1: old friends and recent additions. *Cold Spring Harb Symp Quant Biol* **76**, 211-216 (2011).
77. Clemencon, B., Babot, M. & Trezeguet, V. The mitochondrial ADP/ATP carrier (SLC25 family): pathological implications of its dysfunction. *Mol Aspects Med* **34**, 485-493 (2013).

78. Graham, B.H. *et al.* A mouse model for mitochondrial myopathy and cardiomyopathy resulting from a deficiency in the heart/muscle isoform of the adenine nucleotide translocator. *Nat Genet* **16**, 226-234 (1997).
79. Wang, X. & Chen, X.J. A cytosolic network suppressing mitochondria-mediated proteostatic stress and cell death. *Nature* **524**, 481-484 (2015).
80. Liu, Y. *et al.* Mitochondrial carrier protein overloading and misfolding induce aggresomes and proteostatic adaptations in the cytosol. *Mol Biol Cell* **30**, 1272-1284 (2019).
81. Thompson, K. *et al.* Recurrent De Novo Dominant Mutations in SLC25A4 Cause Severe Early-Onset Mitochondrial Disease and Loss of Mitochondrial DNA Copy Number. *Am J Hum Genet* **99**, 860-876 (2016).
82. Park, K.P. *et al.* SLC25A4 and C10ORF2 Mutations in Autosomal Dominant Progressive External Ophthalmoplegia. *J Clin Neurol* **7**, 25-30 (2011).
83. Hua, Y., Laserstein, P. & Helmstaedter, M. Large-volume en-bloc staining for electron microscopy-based connectomics. *Nat Commun* **6**, 7923 (2015).
84. Pachitariu, M. & Stringer, C. Cellpose 2.0: how to train your own model. *Nat Methods* **19**, 1634-1641 (2022).
85. Stringer, C., Wang, T., Michaelos, M. & Pachitariu, M. Cellpose: a generalist algorithm for cellular segmentation. *Nat Methods* **18**, 100-106 (2021).
86. Chiu C-L, C.N. napari: a Python Multi-Dimensional Image Viewer Platform for the Research Community. *Microscopy and Microanalysis* **28**, 1576-1577 (2022).
87. Thomas Lewiner, H.L., Antonio Wilson Vieira and Geovan Tavares Efficient implementation of Marching Cubes' cases with topological guarantees. *Journal of Graphics Tools* **8**, 1-15 (2003).
88. Wadell, H. Volume, shape, and roundness of quartz particles'. *The Journal of Geology* **43**, 250-280 (1935).
89. Wieckowski, M.R., Giorgi, C., Lebiedzinska, M., Duszynski, J. & Pinton, P. Isolation of mitochondria-associated membranes and mitochondria from animal tissues and cells. *Nat Protoc* **4**, 1582-1590 (2009).
90. Hollenbach, A.D., McPherson, C.J., Lagutina, I. & Grosveld, G. The EF-hand calcium-binding protein calmyrin inhibits the transcriptional and DNA-binding activity of Pax3. *Biochim Biophys Acta* **1574**, 321-328 (2002).
91. Milne, S.B., Mathews, T.P., Myers, D.S., Ivanova, P.T. & Brown, H.A. Sum of the parts: mass spectrometry-based metabolomics. *Biochemistry* **52**, 3829-3840 (2013).
92. Doppler, M. *et al.* Stable Isotope-Assisted Plant Metabolomics: Combination of Global and Tracer-Based Labeling for Enhanced Untargeted Profiling and Compound Annotation. *Front Plant Sci* **10**, 1366 (2019).
93. Malik, A.N., Czajka, A. & Cunningham, P. Accurate quantification of mouse mitochondrial DNA without co-amplification of nuclear mitochondrial insertion sequences. *Mitochondrion* **29**, 59-64 (2016).
94. Hallett, P.J., Collins, T.L., Standaert, D.G. & Dunah, A.W. Biochemical fractionation of brain tissue for studies of receptor distribution and trafficking. *Curr Protoc Neurosci* **Chapter 1**, Unit 1 16 (2008).
95. Muller, L., Kutzner, C.E., Balaji, V. & Hoppe, T. In Vitro Analysis of E3 Ubiquitin Ligase Function. *J Vis Exp* (2021).

Editor's Summary

In skeletal muscle mitochondria, CRL5Ozz and Alix regulate the levels of the ATP transporter Slc25A4; loss of either protein in mice alters Slc25A4, causing mitochondrial defects, metabolic changes, and a shift from oxidative to glycolytic fibers.

Peer review statement

Communications Biology thanks the anonymous reviewers for their contribution to the peer review of this work. Primary Handling Editors: Giulia Bertolin and Dario Ummarino. A peer review file is available.

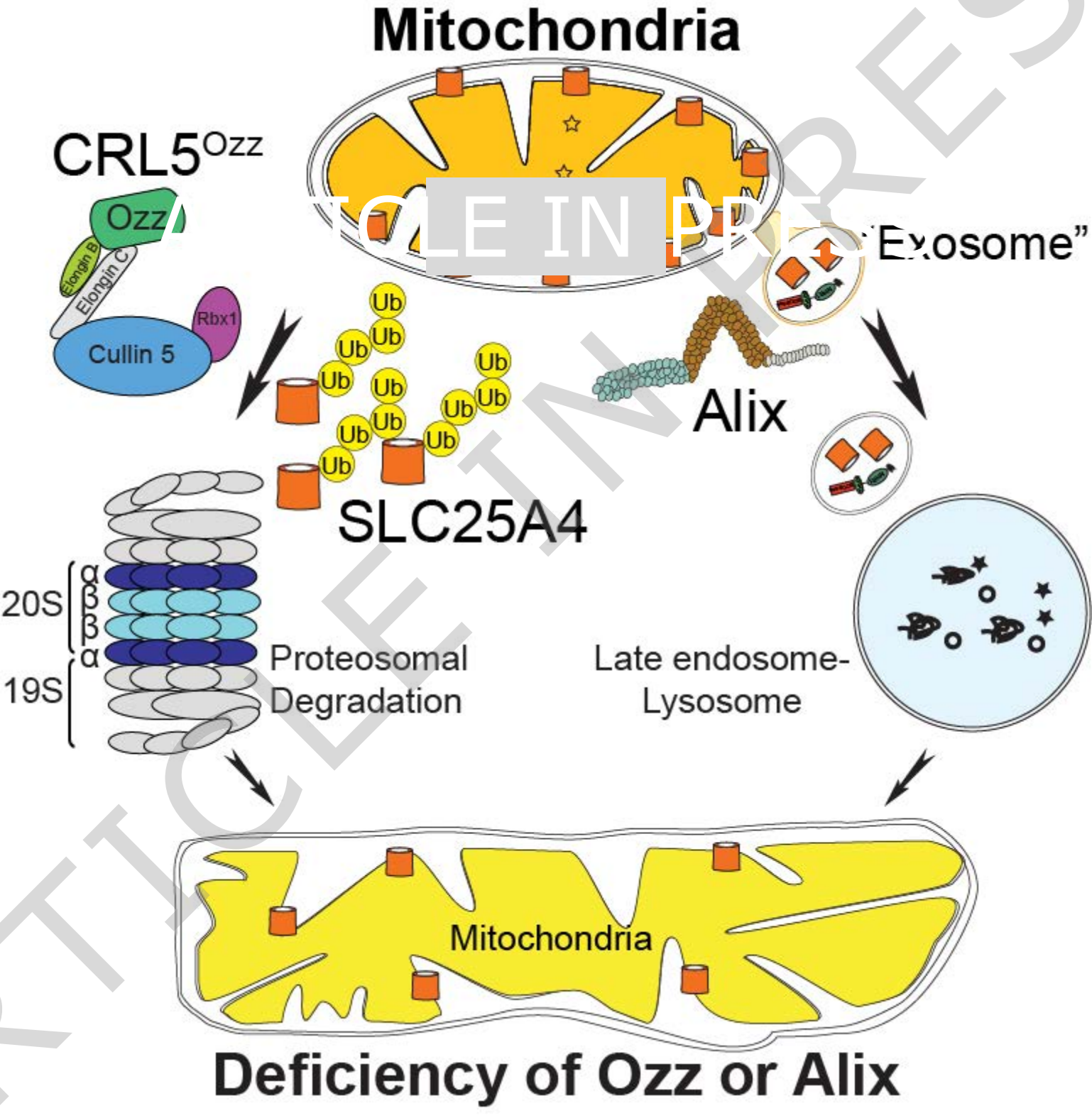
Mitochondria
CRL5Ozz
Ozz
Elongin B
Elongin C
Rbx1
Cullin 5
Ub
SLC25A4
"Exosome"
Alix
20S
19S
α
β
Proteosomal
Degradation
Late endosome-
Lysosome
Mitochondria
Deficiency of Ozz or Alix

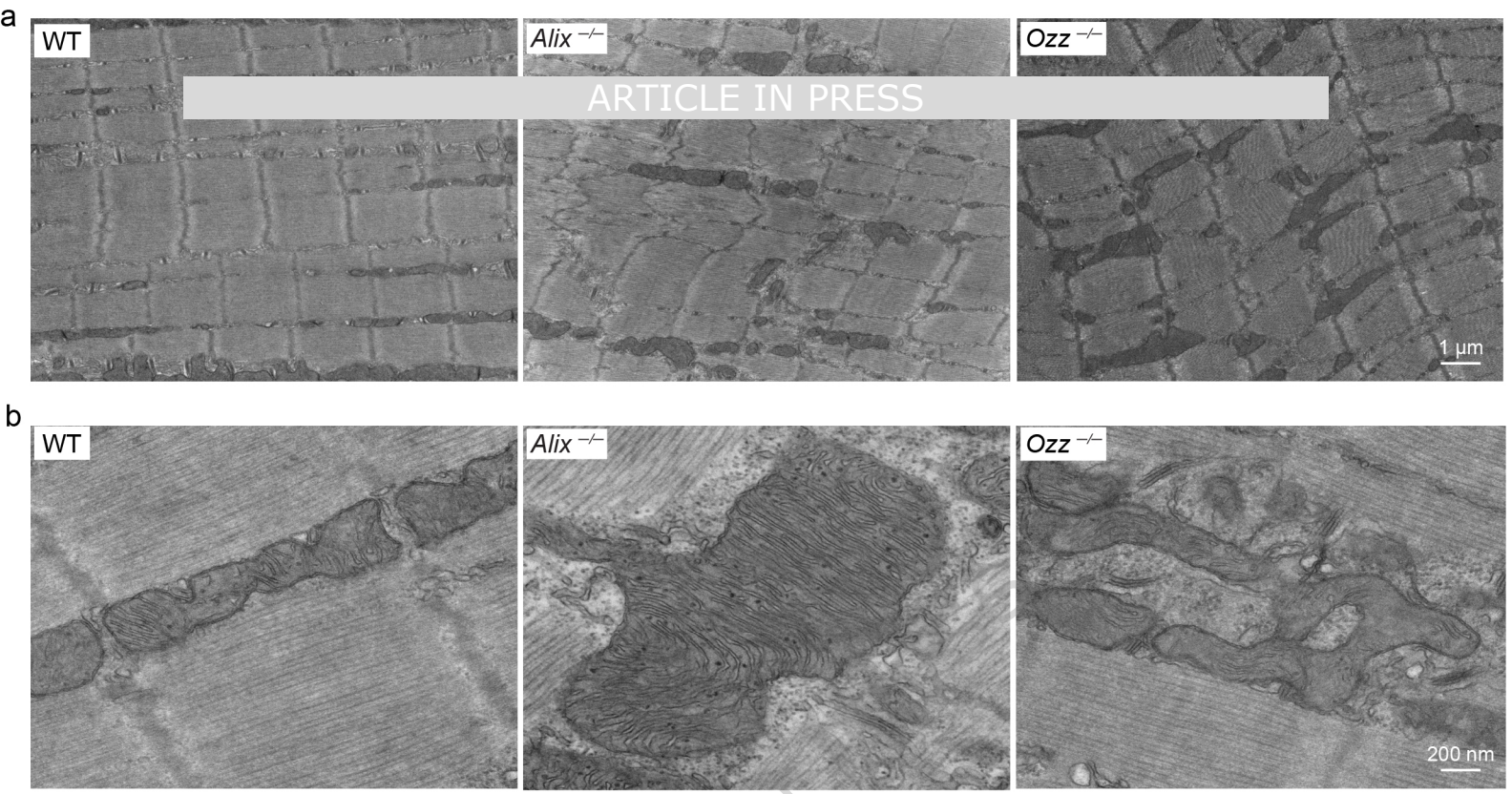

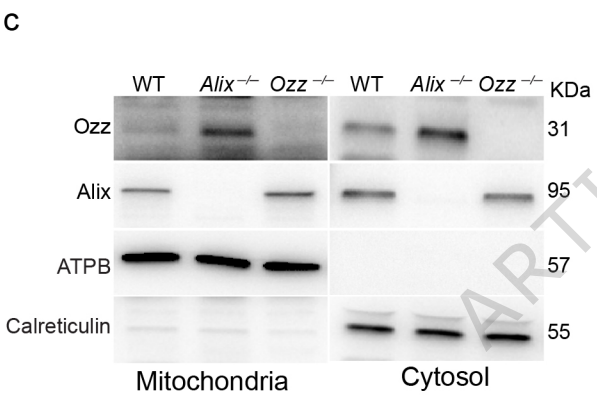

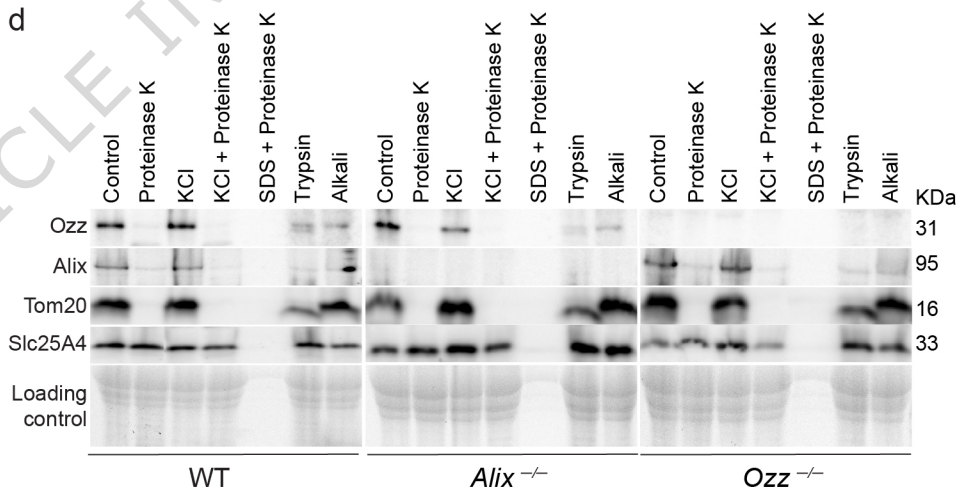

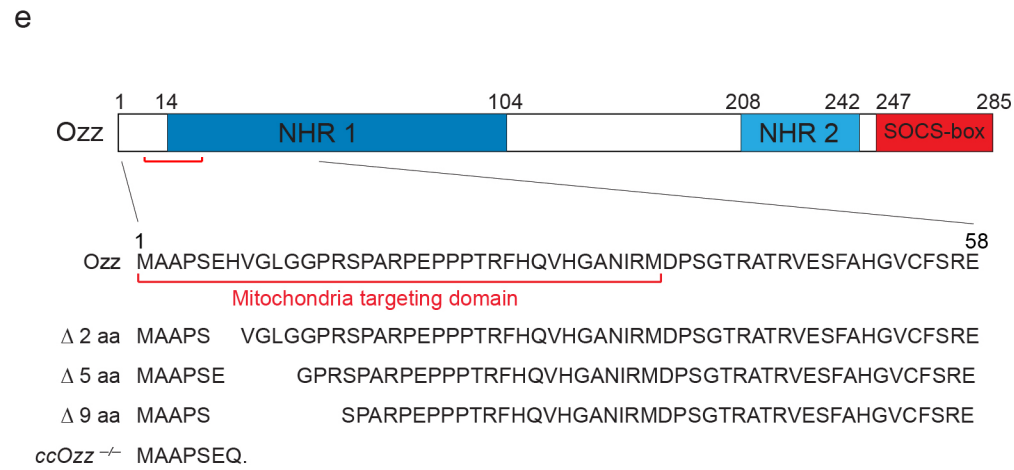

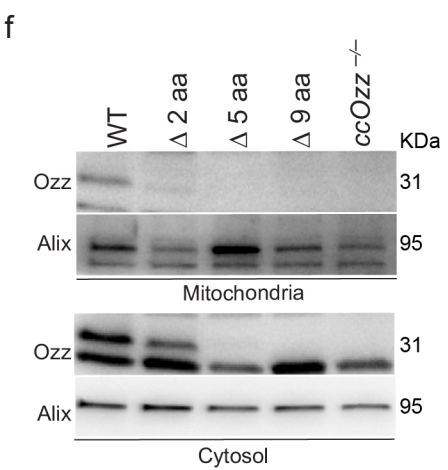

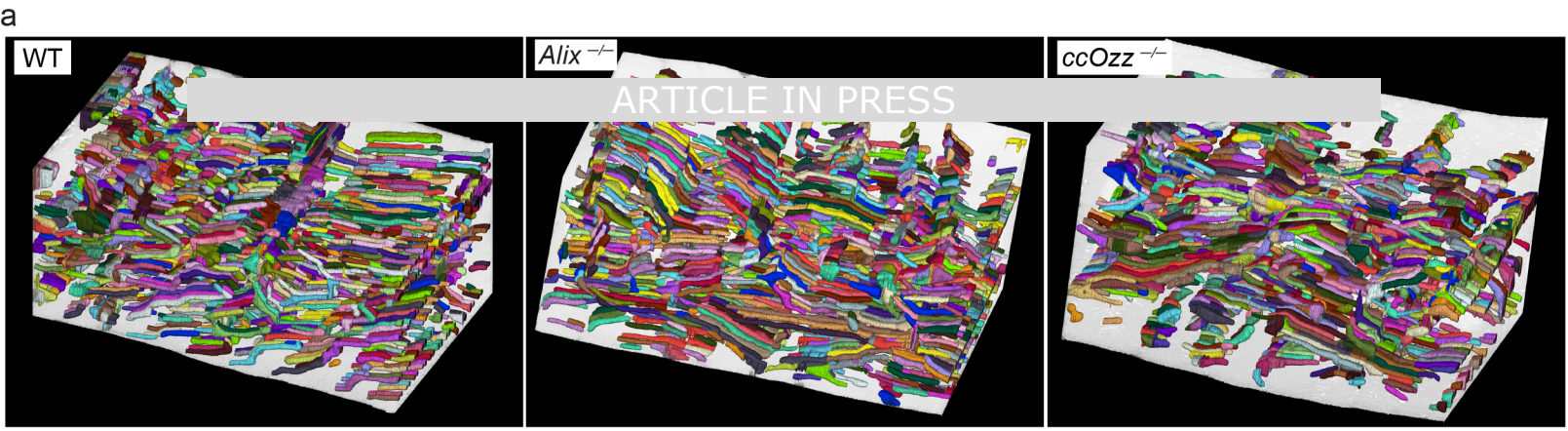

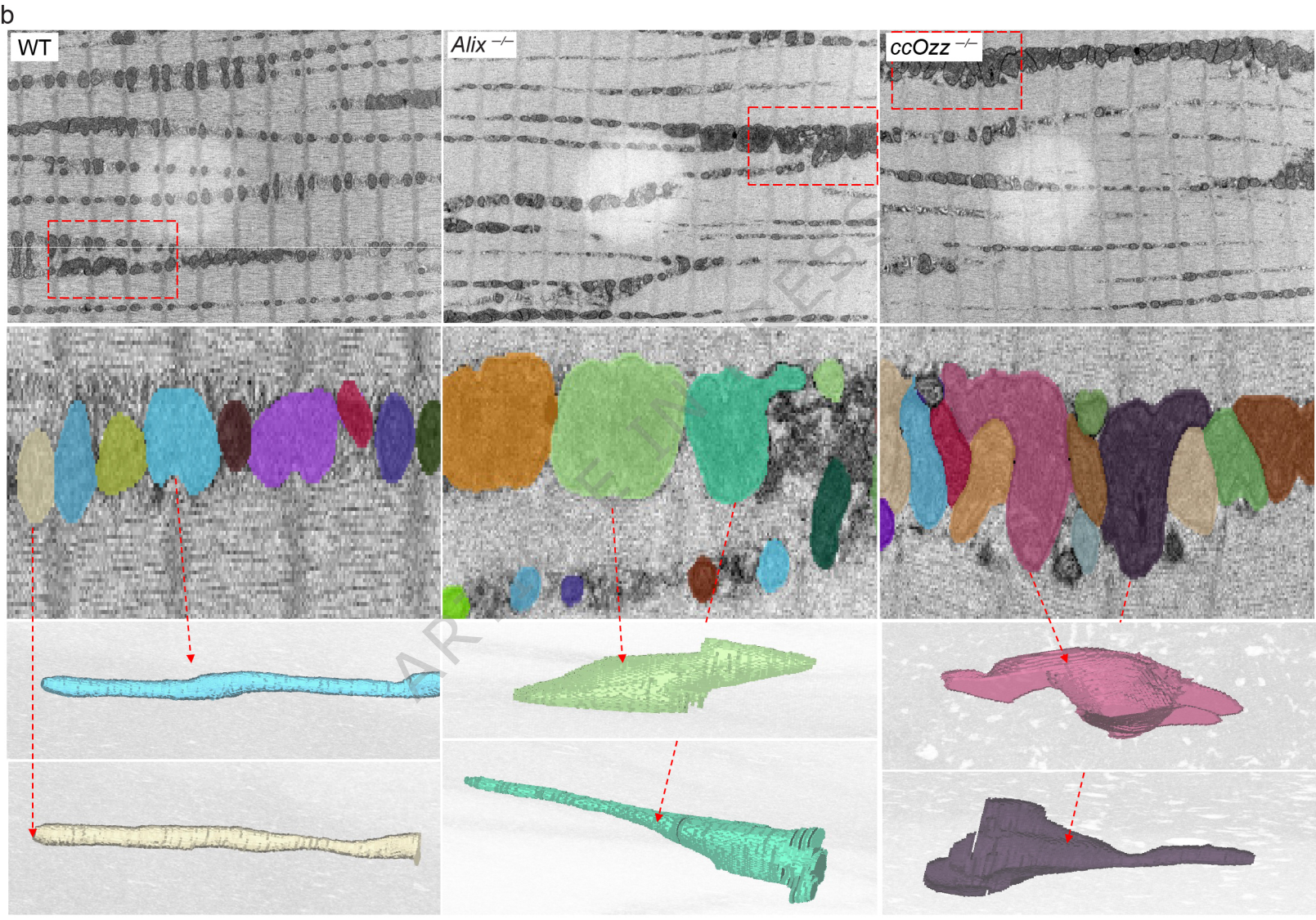

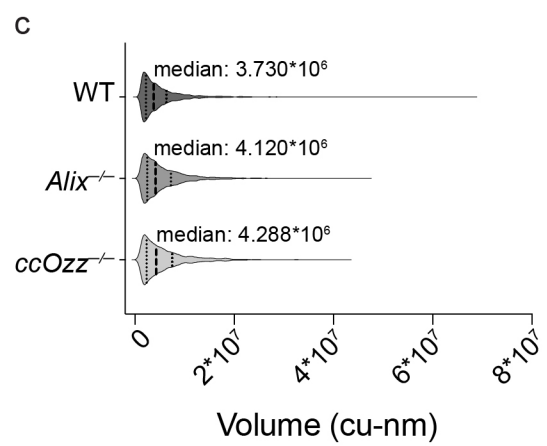

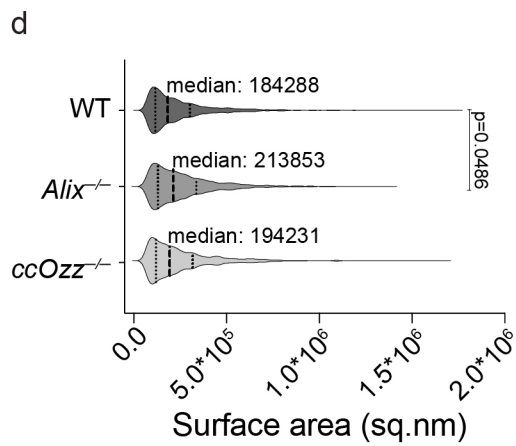

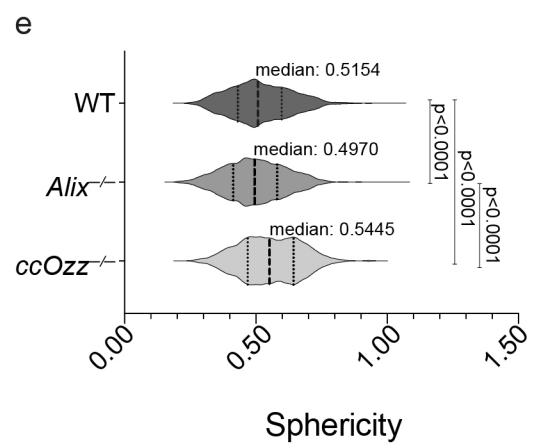

Fig. 3

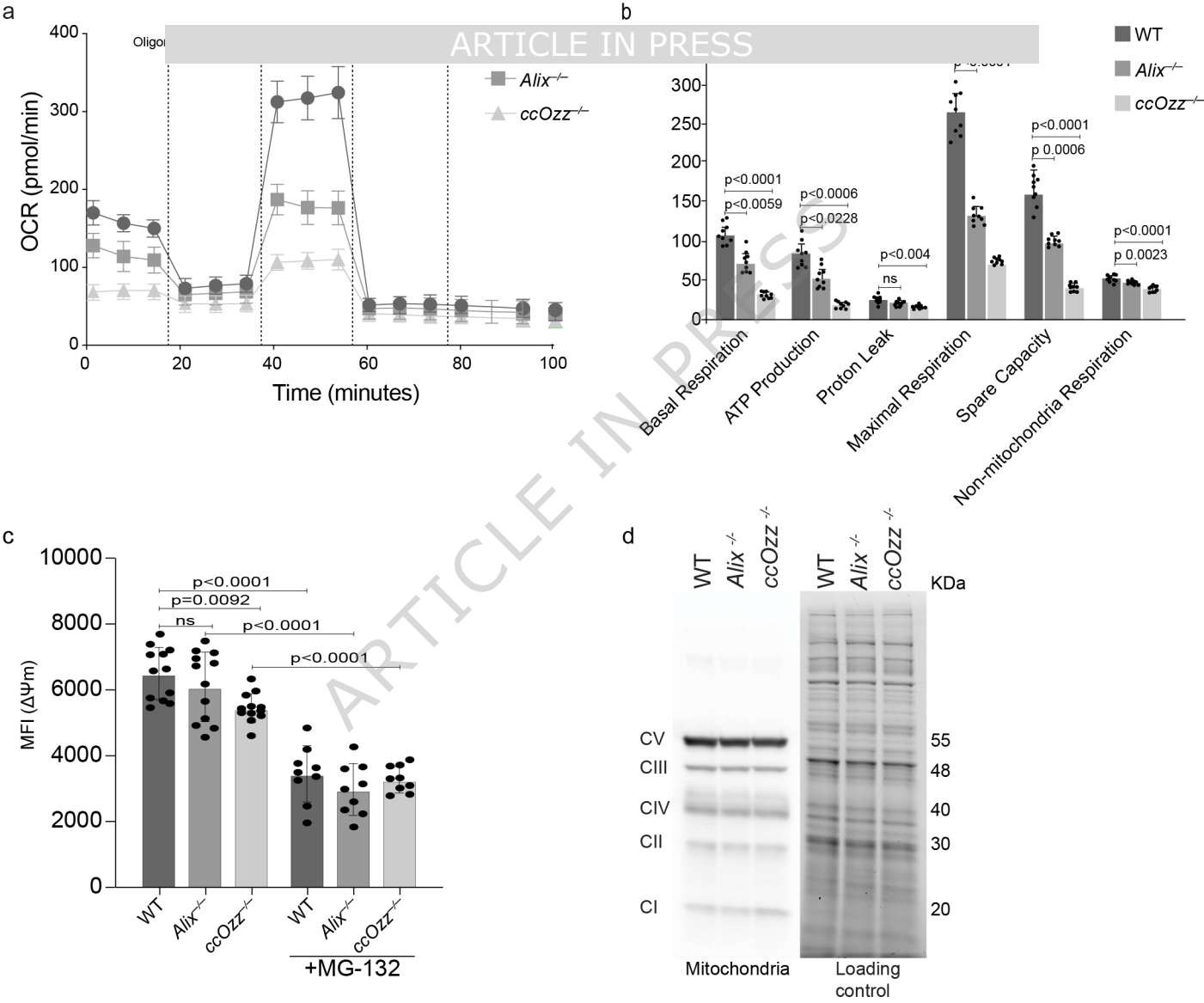

a

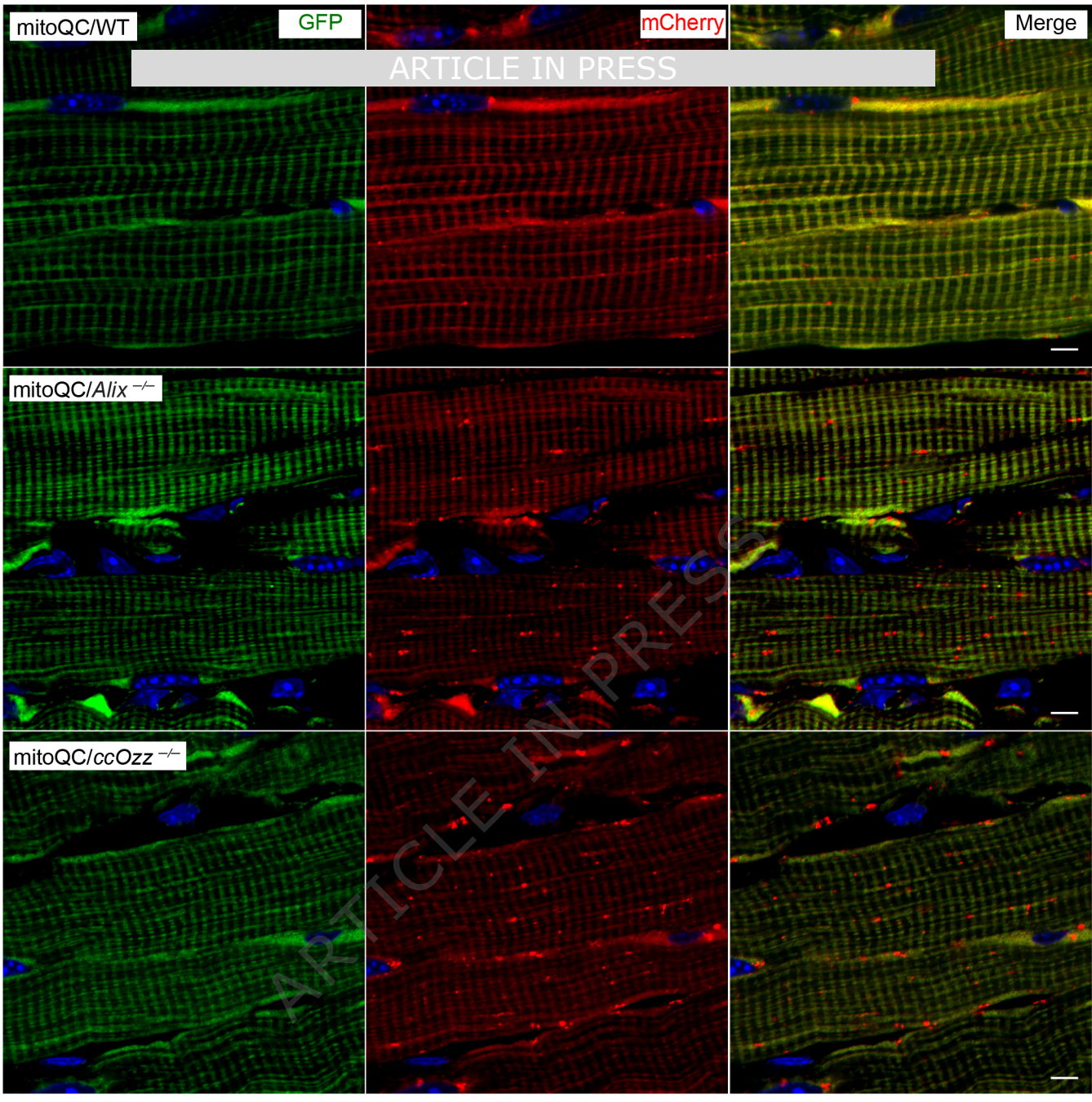

b

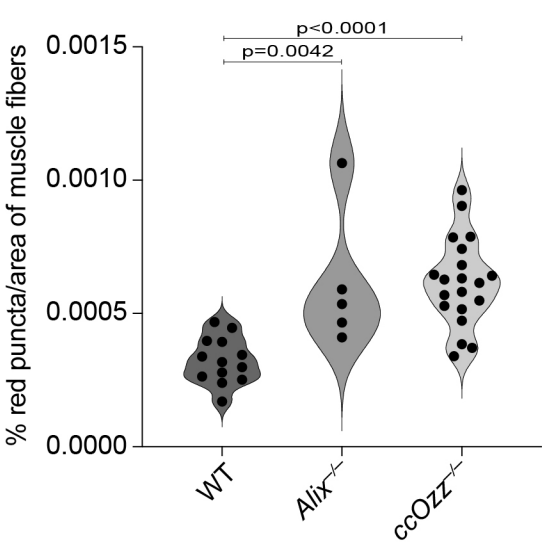

Fig. 5